



On Interactions of Extragalactic Objects

Ondrej Urban

May 2011

Department of Theoretical Physics and Astrophysics
Masaryk University

A great number of people – be it directly or indirectly – contributed to this thesis. First and foremost the huge thank you goes to Norbi and Aurora for being great supervisors during the working day and adoptive parents during the remaining time (and for letting me quote a comic book during the speech at their wedding). Then there is Filip for coping with my dubious communication skills and still helping me bear this to the hard-cover end. Sis for free therapy, real life, broccoli and bananas. My roommates for creating the coziness. IAYC people, at the very least because without them this wouldn't be in English. And parents – I hope the trips to California will make up for all the stuff you invested in me.

The author acknowledges the support of the applied research project financed by the Masaryk University MUNI/A/0968/2009.

I declare that I have written my diploma thesis on my own and using exclusively the cited resources. I agree with lending of the thesis and making it public.

Brno, 13th May 2011

Ondrej Urban

Contents

1	Introduction to the Galaxy Clusters	5
1.1	Motivation	7
1.1.1	Cosmological Importance of the Galaxy Clusters	7
1.2	Observations	9
1.2.1	Radio Observations	9
1.2.2	Sunyaev-Zel'dovich Observations	11
1.2.3	Optical Observations	12
1.3	History	13
2	Intracluster Medium	15
2.1	Physical Properties of the ICM	15
2.1.1	ICM in Kinetic Equilibrium	16
2.1.2	ICM as Plasma in Collisional Ionisation Equilibrium	17
2.1.3	ICM as Plasma in Excitation Equilibrium	18
2.2	ICM Emission	18
2.2.1	Continuum Emission	18
2.2.2	Line Emission	20
2.2.3	Physical Properties From the ICM X-ray Spectrum	21
2.3	Historical Remarks	21
3	ICM Across the Cluster Volume	23
3.1	ICM in the Galaxy Clusters	23
3.1.1	Temperature of the ICM	25
3.1.2	Metallicity of the ICM	26
3.1.3	Properties Obtained by Deprojection	28
3.2	Observing the ICM Out to the Virial Radius	29
3.3	XMM-Newton	31
4	Virgo Cluster Out to the Virial Radius	33
4.1	Observations and Data Reduction	33
4.1.1	Data Analysis	33
4.1.2	Spectral Analysis	35
4.2	Results	37
4.2.1	X-ray Surface Brightness	37
4.2.2	Spectral Results	37
4.2.3	Systematic Errors	41
4.3	Discussion	44
4.3.1	The Unrelaxed Outskirts of a Forming Cluster	44
4.3.2	Metals in the Outskirts	49
5	Conclusions	51

Abstract

Galaxy clusters represent one of the hottest topics in the present-day astrophysics, both observational and theoretical. In the first part of the thesis we discuss the motivation for their studying and some of the most interesting results. We mostly focus on the clusters' observational X-ray properties. The emission in these energies comes from hot diffuse gas continuously filling the cluster gravitational potential – the so-called intracluster medium. We describe its physical properties and how these vary within a given galaxy cluster.

Since the practical part of the thesis is focused on studying the intracluster medium in the cluster outskirts we discuss the recent effort in the field in more detail and briefly describe the *XMM-Newton* satellite, whose data we used.

In the practical part we present the analysis of 13 *XMM-Newton* pointings of the Virgo cluster covering it from the center out to the radius ~ 1.2 Mpc ($\sim 4.5^\circ$) – to the virial radius and beyond. This is the first time the properties of a dynamically young unrelaxed galaxy cluster have been studied in its outskirts. We find the electron density profile can be described by a power-law $n_e \propto r^{-\beta}$ with $\beta = 1.21 \pm 0.12$. In the interval $0.3 r_{\text{vir}} < r < r_{\text{vir}}$ the best fit temperature drops by 60 percent. Within $r < 450$ kpc the entropy can be described by the power law $K \propto r^{1.1}$, outside this radius the entropy flattens out keeping below the expected value by the factor of 2 – 2.5. This shallow density profile and flattening of the entropy can be most probably be described by the clumping of the ICM at the large radii. We also find that the ICM is enriched to the value of at least $\sim 0.1 Z_\odot$ all the way to the virial radius.

*Pray look better, Sir...
those things yonder are no giants,
but windmills.*

– Miguel de Cervantes



Introduction to the Galaxy Clusters

As it turns out, the Universe at its largest scales is not that different from the foam when we take a bubble bath. Huge spans of empty space are surrounded by walls of higher density, creating the “bubbles”. At times these bubbles intersect, creating what we call the filaments of the cosmic web. At the intersections of these filaments we find the galaxy clusters. Fig. 1.1 shows a part of the Millennium simulation with the filaments and the galaxy clusters¹.

Being the largest gravitationally bound objects in the Universe with the radii of 1 – 2 Mpc, the galaxy clusters have been capturing the human curiosity since almost a century ago when we started gathering detailed knowledge about them. Their sheer size grants them properties that enable us to use them as cosmology probes, find out about the chemical evolution of the whole Universe as well as witness the most energetic processes second only to the Big Bang itself – the cluster mergers.

Each new window in the electromagnetic spectrum that the mankind opened has contributed to the knowledge about the galaxy clusters. From the dawn of the X-ray observations in the 1960’s, when the first signs of the hot gas filling the potential of the cluster (*intracluster medium*, ICM, see Chap. 2) appeared, we discovered a plethora of interesting and – given the size of the clusters – extreme phenomena. At the time of writing the latest contribution to the family of extremes are the megaparsec-sized shock arcs moving through the cluster’s hot gas, especially prominent in the lowest frequencies of the spectrum due to their steep power-law spectrum. New instruments like LOFAR² are expected to shed new light on these objects.

In this chapter we discuss in some detail the motivation to study the galaxy clusters, briefly mentioning some of the interesting cosmology results (cf. Sect. 1.1), give some examples of the observational possibilities (Sect. 1.2) and finish the chapter by mentioning a couple of historical remarks (Sect. 1.3).

¹The simulation was carried out using only the dark matter particles. Even though the baryonic – and thus radiating – matter follows the dark matter distribution, the various brightness levels represent various densities of the dark matter clouds.

²<http://www.lofar.org/>

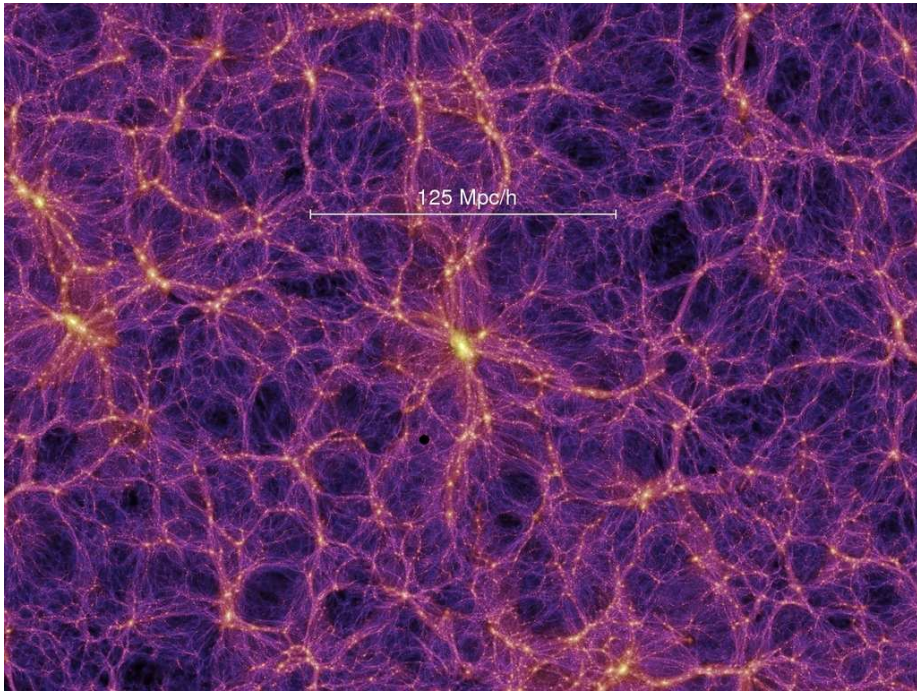


Figure 1.1: Cutout from the Millennium Simulation Project result. 10 billion dark matter particles filling the cubic region of 2 billion light years were used in the simulation. We clearly see the voids, filaments and the galaxy clusters. (Springel et al., 2005)

1.1 Motivation

There is a broad range of science in general and astrophysics in particular to which the research of the galaxy clusters significantly contributes. In this section we first briefly list the general reasons for studying these objects and follow with mentioning some of the most important results of cosmological importance.

Clusters of galaxies exhibit several superlatives. Following the list by Böhringer and Werner (2010) these are:

1. the ICM being the hottest plasma in thermal equilibrium we can study (detailed discussion in Chap.2)
2. the largest light deflection in the deep potentials of the clusters gives rise to spectacular gravitational lensing effects
3. the cloud of hot ICM casts the darkest shadow on the cosmic microwave background via the Sunyaev-Zel'dovich effect
4. cluster mergers, with energies up to $\sim 10^{63}$ erg are the most energetic processes in the Universe, outdone only by the Big Bang (Feretti et al., 2002)

The first three points cover the three areas in which the cluster observational effort is the most active these days. We discuss them in more detail in Sec. 1.2.

1.1.1 Cosmological Importance of the Galaxy Clusters

Undoubtedly one of the biggest contribution of the galaxy cluster research is that to the observational cosmology.

The most obvious example is using the cluster properties as independent probes for determining the cosmological parameters of the Universe. Probably the most straightforward method of achieving this is using the population of the clusters at different redshifts to infer the amount of clumping and thus the underlying cosmology. Looking at clusters as perturbations in otherwise homogeneous Universe, we can study their abundance throughout the history. Wang and Steinhardt (1998) use the rich cluster abundance to study the relations between the parameters σ_8 (density perturbations on $8h^{-1}$ Mpc scale, where $h = H_0/100 \text{ km s}^{-1} \text{ Mpc}^{-1}$), Ω_m (fraction of matter in the Universe) and w (equation of state of the dark energy), also looking for ways how to use the constraints to determine the correct cosmology.

Galaxy clusters, owing to their size, offer a representative sample of the composition of the Universe. As proposed by Sasaki (1996) and Pen (1997) the fraction of the hot X-ray emitting gas mass to the total cluster mass – $f_{\text{gas}} = M_{\text{gas}}/M_{\text{tot}}$ can be used as a cosmological probe. Since we are not aware of a process that could change this fraction over the \sim Mpc scales of the galaxy clusters, it should remain constant with varying (resp. growing) redshift z . However, since $M_{\text{gas}}/M_{\text{tot}}$ depends on the adopted cosmological parameters (through

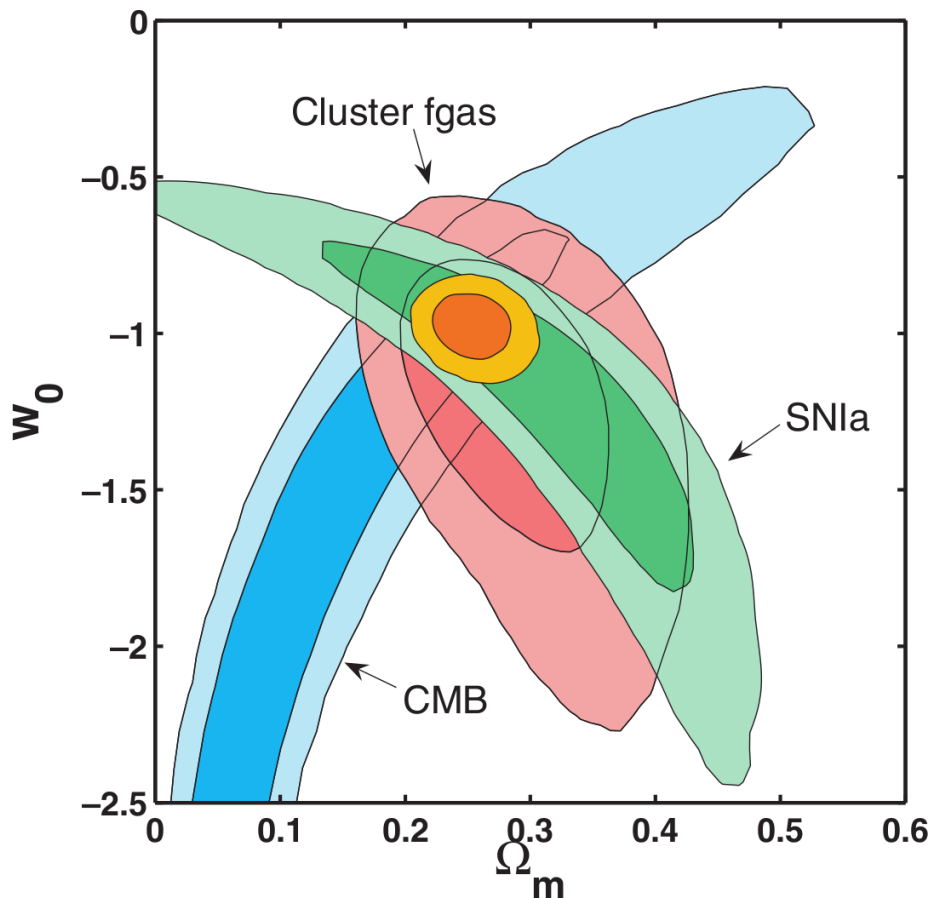


Figure 1.2: 1 and 2σ confidence constraints in the (Ω_m, w) plain. The assumption of a flat cosmology with a constant dark energy equation of state w holds. (Allen et al., 2008)

the cluster's angular diameter distance) we can use the $f_{\text{gas}}(z)$ measurements to determine these. Allen et al. (2004) use 26 *Chandra* clusters ($0.07 < z < 0.9$) to study the Λ CDM model³ parameters $\Omega_m = 0.26^{+0.06}_{-0.04}$, $\Omega_X = 0.75 \pm 0.04$ and $w_X = -1.26 \pm 0.024$. Recently Allen et al. (2008) improved the constraints by using 42 hot ($T > 5$ keV) clusters, having also expanded the redshift range $0.05 < z < 1.1$. Combining their findings with the independent results from the supernova Ia (SN Ia) studies and the cosmic microwave background measurements they find $\Omega_m = 0.253 \pm 0.021$ and $w = -0.98 \pm 0.07$ for the flat cosmology. The various confidence regions are shown in Fig. 1.2.

Apart from determining the cosmological parameters, galaxy clusters can be

³In these models the equation of state for the dark energy w_X is allowed to take any value as opposed to the Λ CDM cosmology with $w = -1$.

used to challenge various cosmological theories as famously demonstrated by the *Chandra* observation of 1E 0657 – 558, the so-called Bullet cluster. Apart from being one of the hottest clusters known it also contains a cluster merger almost in the plane of the sky. Clowe et al. (2004) use the combination of the X-ray and weak gravitational lensing (cf. Sec. 1.2.3) observations to offer one of the strongest proofs of the existence of the dark matter and challenge the MOND theory (Milgrom, 1983). Assuming the collisionless nature of the dark matter, the cluster collision in the Bullet cluster separated the cluster components – the galaxies and the underlying dark matter on one hand, which were affected only weakly by the merger, and the cloud of the hot X-ray emitting gas on the other, which got slowed down. Traditional X-ray and optical observations indeed show separated peaks of the distributions of the galaxies and the hot gas respectively. Weak lensing then allows to reconstruct the underlying mass profile, putting the mass peak near the galaxy distribution peak with high (3.4σ) significance, strongly suggesting the dark matter interpretation, since the hot gas comprises the majority of the baryonic mass of the galaxy clusters. Bradač et al. (2006) confirm this result as well as for the first time combine strong and weak lensing results to constrain the mass distribution even further. Fig. 1.3 shows the cluster’s mass distribution and X-ray surface brightness overlaid on the optical image – the mass peak offset is clearly visible.

We see that the galaxy clusters are an important cosmological probe with a wide variety of results and conclusions. However their astrophysical and, in fact, physical importance is by far not limited only to the cosmology. We devote the following sections and chapters to show the wide variety of the cluster science with stress of their X-ray characteristics.

1.2 Observations

Galaxy clusters are interesting observational targets across the whole electromagnetic spectrum. The major bands in which they are studied are the radio, visible spectrum and X-rays. The observation of the Sunyaev-Zel’dovich effect technically also falls to the radio band of the spectrum, however due to its inherent differences in the basic principle we devote a separate subsection to the discussion.

Below we discuss each of the above methods of observation except for the X-rays, which will be separately and in bigger detail described in further chapters.

1.2.1 Radio Observations

Radio emission from the galaxy clusters usually originates as synchrotron radiation from the cluster’s relativistic gas which contains electrons with the energies $E = \gamma m_e c^2$ with $\gamma \gg 1000$. Since the synchrotron radiation is emitted by accelerated electron, observing it reveals the presence of magnetic fields in the clusters, whose induction lines the electrons orbit.

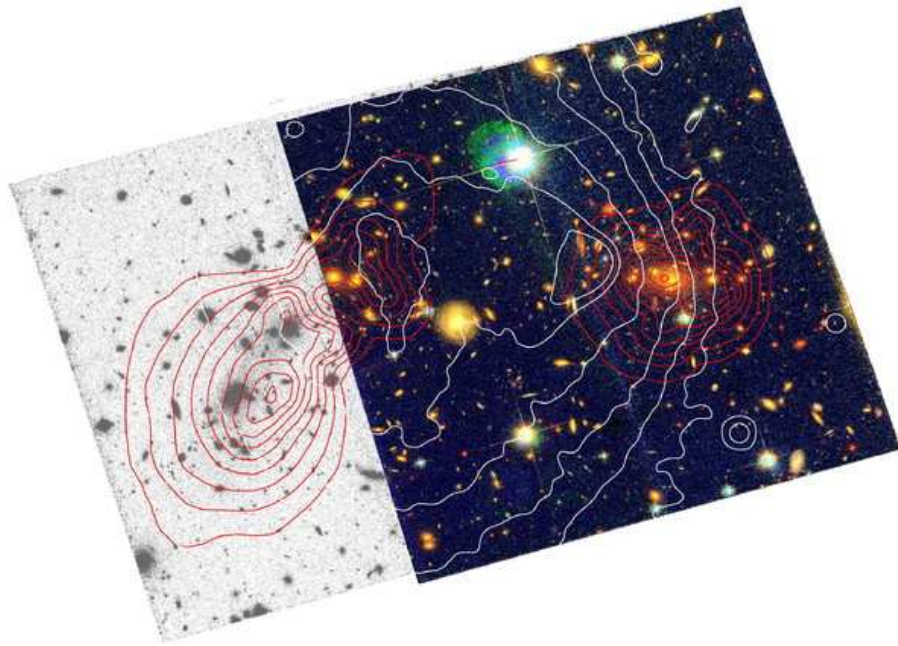


Figure 1.3: A composite of the optical images of the Bullet cluster. Overlaid are the X-ray brightness contours (white) and the mass profile contours from the combination of the strong and weak lensing (red). (Bradač et al., 2006)

The most spectacular aspect of the cluster radio emission comes from the diffuse sources that we cannot directly assign to any member galaxy. This fact suggests that clusters contain magnetic fields on the cluster volume scales. The observation of the diffuse sources can be bound to the optical and X-ray observations to study the cluster history and evolution.

The presence of the diffuse radio sources in clusters is not common. Giant radio halos are present in only about $\sim 5\%$ of the clusters (Giovannini et al., 1999). Taking the relatively short lifetime of the relativistic electrons of $\sim 10^8$ yr (Sarazin, 1999) and a very low diffusion speed of $\sim 100 \text{ km s}^{-1}$ through the ICM, we need to find a way to supply energy to them. This, as it turns out, can be provided by the cluster mergers (for details see the review in Feretti and Giovannini (2008)). Huge ($\gtrsim 1$ Mpc) radio relics that can be found in the clusters are also supposed to be the result of mergers.

Studying the radio halos of the individual galaxies also leads to exciting results. The hot ICM, through which the galaxy is moving, deforms the halo, allowing us to directly study the interaction between the both, revealing the tail-like structures spanning behind the galaxies.

Centers of the cooling core clusters (see Chap. 3) can contain radio structures as well – large X-ray cavities filled with relativistic gas, which show up dark in the X-ray images.

Studying the cluster radio sources with steep power-law spectra is expected to expand in the future thanks to new instruments like LOFAR (the LOW Frequency ARray), that will enable us to observe in as-of-now unexplored extremely low frequencies, making the various exciting radio features brighter by orders of magnitude.

1.2.2 Sunyaev-Zel'dovich Observations

The idea of using the distortion of the cosmic microwave radiation to study the cluster gas was theoretically proposed by Sunyaev and Zeldovich (1972). In their paper they predicted that the cloud of the gas in the cluster gravitational potential is able to inversely-Compton scatter the incoming relict photons, resulting in the upward shift in their energy.

There are two different versions of this Sunyaev-Zel'dovich (SZ) effect – thermal and kinematic. While both are caused by Thompson scattering of the photons on cluster electrons (and as such can be confused with each other in the observations), there is a difference. Thermal SZ effect is caused by a cluster at rest with respect to the cosmic microwave background, while in the case of the latter the motion of the cluster is the reason for the scattering.

While still remaining a rather experimental and young method of cluster studying (see Birkinshaw and Lancaster (2008) for the review and further reference) there is a strong motivation to develop the suitable instrumentation to enable advanced research in the field. SZ effect is (virtually) redshift independent. This potentially gives it a huge advantage when it comes to cluster surveys compared to the X-rays. The X-ray brightness decreases with the distance and

at the large redshifts the only X-ray detectable clusters are the most massive ones, significantly biasing the survey statistics.

Combining the X-ray and SZ studies brings up the possibility of absolute measurements of the distance. The results of the both measurements can be put together to determine the cluster linear dimension, at which point the distance can simply be determined by its angular dimension.

As will be discussed in the main results of the thesis, using SZ observations in combination with the X-ray can shed some light on the properties of the density clumps in the cluster's hot gas in the cluster outskirts.

1.2.3 Optical Observations

We can distinguish three main objectives when observing the galaxy clusters in the visual part of the spectrum. First is the studying of the galaxies themselves, their evolution within the clusters and so on. This is of only marginal interest to us in the study of the clusters as whole and we will not discuss this further. We can however briefly mention the visual sky surveys as the basis for constructing the cluster catalogues. In the end of the subsection we discuss the gravitational lensing as an important tool for studying of the clusters.

Optical studies are, due to their long history and the low cost at the present time, useful in the cluster detection and catalogization. Systematic studies of the large areas of the sky for the galaxy clusters begun in the second half of the 20th century. Abell (1958) used the Palomar Observatory Sky Survey photographic plates to detect galaxy clusters, using strict rule to ensure a statistically homogeneous sample. His catalogue of 2712 clusters remains to this day as the most famous galaxy cluster catalogue.

Further studies made use of developing technology and gradually started employing first digitalized and subsequently digital data and numerous computer algorithms to detect clusters. A good review of this is given by Gal (2008).

Gravitational lensing as a method to study galaxy cluster masses has been suggested already by Zwicky (1937). As one of the results of the then recently proven general theory of relativity, the path of a light ray from the distant sources passing in the vicinity of a massive object will be roughly speaking bent by an angle depending on the object's mass⁴. Distorted images of the background sources created in this way can be used to reconstruct the mass distribution of the gravitational lens, the cluster in our case. This method is especially useful as it enables us to map the distribution of the invisible dark matter, comprising the majority of the cluster mass.

The gravitational lensing of the clusters comes in two "flavors". Strong lensing (see Lynds and Petrosian (1986); Soucail et al. (1987) for the early observations) occurs near the cluster centers, where the images of the background get significantly distorted creating arclets and multiple images. Weak lensing (first discovered observationally by Tyson et al. (1990), triggering a series of

⁴To be precise it is important to remark, that Newtonian physics can also explain the bending of the light ray. The general relativity however predicts the angle to be twice the classical result.

theoretical papers during the 90s) comes into play in the cluster outskirts where the distortion of the background sources becomes small. It manifests itself in the major axes of the background elliptical galaxies being predominantly oriented in the perpendicular direction to the cluster core. Statistically mapping the shapes of the background galaxies we can use the non-randomness of their orientation to map the distribution of the matter in the clusters.

1.3 History

In this section we briefly mention a couple of historically important results, papers and efforts that we did not discuss in the above sections.

The observations of the clusters of galaxies go over 200 years to the past⁵. Messier (1784) was the first one to notice the irregularities in the distribution of the nebulae in the sky. However it was W. Herschel to first recognize several clusters and groups of galaxies (most notable the Coma cluster, Leo, Ursa Major etc.; cf. Herschel (1785, 1811)).

Further effort to catalogue the nebulae was accompanied with the discussion of their nature – be it extragalactic or not. This culminated in the Great Debate on 26th April 1920 between H. Shapley and S. Curtis and got finally resolved later by Hubble (1929) who proved that many of the nebulae are extragalactic objects.

Many authors studied the question of the tendency of the galaxies to cluster and the possibility of the existence of even bigger objects (today’s superclusters). Numerous surveys were carried out, the most famous to this day being the Palomar Observatory Sky Survey (POSS), based on which, as mentioned previously, Abell (1958) published his famous catalogue. A notable addition to the galaxy cluster catalogues was announced a year before Abell’s. The *Catalogue of Galaxies and Clusters of Galaxies* was published by Zwicky et al. (1968) but contains a statistically less complete sample of the clusters.

Galaxy clusters offered the first indication for the existence of the dark matter. In his famous paper Zwicky (1937) used the virial theorem and the assumption of relaxation stability of the Coma cluster to conclude it contains much more mass than the mere sum of the masses of all the galaxies. Big effort has been made to offer an alternative explanation than the “hidden mass”, including H I filling the cluster potential (theoretically argued for by Stone (1955)), alternative theories of gravitation (Zwicky, 1957) and so on. The observational effort was summarized by de Vaucouleurs (1960), concluding the necessity of the existence of some kind of dark bodies. The idea of the dark matter consisting of diffuse gas started gaining significance. Woolf (1967) observed Abell 2065 and Abell 1656 (Coma cluster) to successfully detect ionized gas. However with the discovery of the diffuse gas in the galaxy clusters (Meekins et al., 1971; Gursky et al., 1971, cf. Chap. 2) it became clear that the diffuse gas could not account for the missing mass. Many theories of the dark matter have been brought up

⁵Detailed discussion of the galaxy cluster research history can be found in the excellent review Biviano (2000).

1.3. HISTORY

following this discovery only to be proven wrong – the baryonic origin of the dark matter has been ruled out by the theory of primordial nucleosynthesis, the theory of the massive collapsed objects (van den Bergh, 1969) was ruled out by the lack of tidal distortions of the galaxies and so on. The search of the true nature of the dark matter is still ongoing.

In general more than two centuries of the galaxy cluster observations have revealed much about themselves, the residing galaxies, the Universe as whole. Many questions have been answered, many more asked and a plenty of issues concerning the objects are among today's hottest topics in astrophysics.

2

Intracluster Medium

The majority of the baryonic mass in a galaxy cluster resides in the areas between the galaxies¹, continuously filling the cluster's gravitational potential in the form of hot plasma we call the *intracluster medium* (ICM).

In this chapter we discuss the physical properties of the ICM (Sect. 2.1), describe how its emission looks in general (Sect. 2.2) and briefly look at the historical progress of its discovery and exploration (Sect. 2.3).

2.1 Physical Properties of the ICM

Even though appearing empty in the optical images, the vast stretches of space between the galaxies in the clusters are filled with matter. The intracluster medium consists of diffuse gas with temperatures of $T \sim 10^7 - 10^8$ K. We therefore usually express its temperature in more convenient keV – $T \sim 1 - 10$ keV. Even though highly rarefied (the electron number densities are in order of $n_e \sim 10^{-4} - 10^{-2} \text{ cm}^{-3}$ decreasing with the distance from the cluster center) the ICM fills the cluster potential wells out to $r \sim \text{Mpc}$ and thus contains a considerable amount of the cluster's baryonic mass, $M_{\text{gas}} \sim 10^{14} M_{\odot}$ ². High temperature of the ICM is due to the deep gravitational potential wells of the clusters and the way the clusters form. It is believed that most of the heating is of the gravitational origin – gas falling to the potential well of the cluster would be accelerated to speeds $\gtrsim 1000$ km/s. When encountering the gas with different speed, they form a shock, heating the infalling gas in the process.

The metal content of the ICM implies that a fraction of the ICM came from the cluster galaxies. The orbiting velocities of these, again of the order of 1000 km/s would lead us to the same conclusion as before. Therefore we can say that the ICM has been heated through merger shocks.

Owing to its high temperature the ICM predominantly radiates in X-rays (even though it's detectable also in other parts of the spectrum). The sheer amount of the ICM particles is responsible for the cluster X-ray luminosities

¹Only about 20% of the baryonic mass forms the stars and galaxies (Jones et al., 2008).

²Baryonic matter is responsible for only about 15% of the cluster mass, the rest consisting of the dark matter.

2.1. PHYSICAL PROPERTIES OF THE ICM

$L_X \sim 10^{43} - 10^{45} \text{ erg s}^{-1}$. Galaxy clusters are therefore the second brightest X-ray emitters in the Universe (after the quasars) and the brightest extended X-ray sources.

As written above, the ICM is polluted by metals. These have been predominantly produced by the stellar population in the member galaxies. For a more detailed discussion on metals in the ICM refer to Subs. 3.1.2.

To completely describe the physical state of the ICM we need to provide (cf. Sarazin (2008)):

- the description of the motions of the free particles (electrons, ions), i.e. the kinetic state of the gas
- specify the ratios of the free and bound electrons, i.e. the ionization state
- know what energy levels do the bound electrons occupy, i.e. the excitation state

2.1.1 ICM in Kinetic Equilibrium

When given enough time the Coulomb collisions in a volume of gas will bring it into kinetic equilibrium, developing the Maxwell distribution in the process. We can express the time scale for a particle of mass m_1 and charge $Z_1 e$ to collide with field particles of mass m_2 and charge $Z_2 e$ in Maxwell distribution of temperature T by (Spitzer, 1956)

$$t_{\text{eq}}(1, 2) = \frac{3m_1 \sqrt{2\pi} (kT)^{3/2}}{8\pi \sqrt{m_2} n_2 Z_1^2 Z_2^2 e^4 \ln \Lambda}, \quad (2.1)$$

where $\ln \Lambda = \ln(b_{\text{max}}/b_{\text{min}}) \approx 40$ is called the Coulomb logarithm with b_{min} and b_{max} being the minimal and maximal impact parameters for the Coulomb collisions in the gas respectively. Under the ICM conditions this parameter is nearly constant.

Plugging in the values for electrons we find that they reach kinetic equilibrium after $t_{\text{eq}}(e, e) \sim 10^5 \text{ yr}$. Naturally the protons take longer, $t_{\text{eq}}(p, p) \approx \sqrt{m_p/m_e} t_{\text{eq}}(e, e)$; a factor of about 43, so $t_{\text{eq}}(p, p) \sim 4 \times 10^6 \text{ yr}$. It takes the longest for the protons and the electrons to exchange the energy among themselves, $t_{\text{eq}}(p, e) \approx (m_p/m_e) t_{\text{eq}}(e, e)$, or about 1870-times longer; $t_{\text{eq}}(p, e) \sim 2 \times 10^8 \text{ yr}$. About half this time is needed for both species to come to equipartition (equal temperatures).

Given the age of the clusters of $\gtrsim 10^9 \text{ yr}$ we can expect the various species of the free particles in the ICM to be in Maxwell distributions and moreover to be in equipartition, $T_e = T_p = T$. Exceptions might occur in the low-density cluster outskirts or the areas of recent significant changes in the gas properties (e.g. shocks).

2.1.2 ICM as Plasma in Collisional Ionisation Equilibrium

Low density and high temperature of the ICM allow one to describe it with a relatively simple model of plasma in the *collisional ionisation equilibrium* (CIE). Two assumptions are made, namely that the plasma is optically thin to its own radiation and that there is no external radiation field to affect its state.

The most important ionisation process under these conditions is the collisional ionisation (photo ionisation and the Compton ionisation³ are neglected by the CIE assumption). The recombination occurs via the radiative and dielectronic recombination. In the latter process a free electron gets captured by an ion and the gained energy is used to excite one of the already bound electrons to a higher energy level. The ion can then get back to the ground level by either auto-ionisation or by emitting a photon.

It is important to note that the ionisation and the recombination in the ICM are not inverse processes and thus the ionisation state of the gas is not thermodynamic equilibrium – we can't use the Saha equation to describe its state. Employing the notation of Sarazin (2008) we let $C(X^i, T)$ be the rate coefficient for collisional ionisation out of the ion X^i (number of ionisations per unit time and unit volume) and $\alpha(X^i, T)$ be the rate coefficient of the recombination to the ion X^i (defined analogically). In CIE the ionisation and recombination processes need to balance out, we can therefore write

$$[C(X^i, T) + \alpha(X^{i-1}, T)] n(X^i) = C(X^{i-1}, T) n(X^{i-1}) + \alpha(X^i, T) n(X^{i+1}), \quad (2.2)$$

where $n(X^i)$ stands for the number density of the ion X^i . To account for the neutral atom we write

$$\alpha(X^1, T) n(X^1) = C(X^0, T) n(X^0). \quad (2.3)$$

Solving the equation 2.3 by choosing an arbitrary value for $n(X^0)$ we can substitute the solution to the Eqn. 2.2 and by induction obtain

$$n(X^{i+1}) = n(X^i) \frac{C(X^i, T)}{\alpha(X^{i+1}, T)}. \quad (2.4)$$

Everything needs to be normalized, i.e. $\sum_{i=0}^Z n(X^i) = n_{\text{element}}$, where the value of the right-hand side is determined by the total plasma density and the element abundance.

Unlike the thermodynamic equilibrium described by the Saha equation the CIE ionisation states don't depend on the density, only on the temperature T . Fig. 2.1 shows the ion concentrations at different temperatures for two important elements, O and Fe. We see that at the cluster temperatures the oxygen is almost completely ionized and only iron retains some of the electrons.

³The process at which an incoming photon is Compton-scattered by a bound electron.

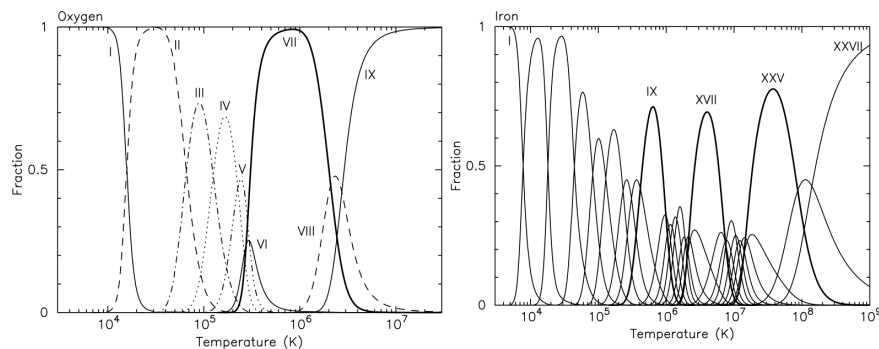


Figure 2.1: Ion concentrations of oxygen (*left*) and iron (*right*) for various temperatures of plasma in CIE. Thick lines mark the ions with completely filled shells. (Kaastra et al., 2008)

2.1.3 ICM as Plasma in Excitation Equilibrium

The excitation state of the ICM is mainly determined by the balance between the collisional excitation and radiative deexcitation. Deexcitation rates are in general much higher than the excitation ones and most of the ions are found in their ground level. Unlike the thermodynamic equilibrium, where the population of the excited ions would be described by the Boltzmann distribution, in the ICM the population of the excited states is much lower.

X-ray spectroscopy cannot be used to determine the density of the gas since the collisional deexcitation rates are much lower than the radiative ones.

2.2 ICM Emission

With the basic physical properties of the ICM described in Sect. 2.1 we can now proceed to how they translate into the spectral features (or equivalently how the spectrum of the ICM allows us to describe its properties).

The spectrum of the ICM contains the usual components – the continuum emission and the spectral lines. The absorption features of the spectrum are of minor interest here since CIE model doesn't work with them (the only exception are the resonant lines in the cluster centers but the focus of the main part of the thesis is not on them).

2.2.1 Continuum Emission

Three processes play the dominant role in creating the continuum emission of any plasma: bremsstrahlung, free-bound emission and two-photon emission. At the temperatures of the ICM the last two don't play a big role (as demonstrated in Fig. 2.2) and we mention them here just briefly.

2.2. ICM EMISSION

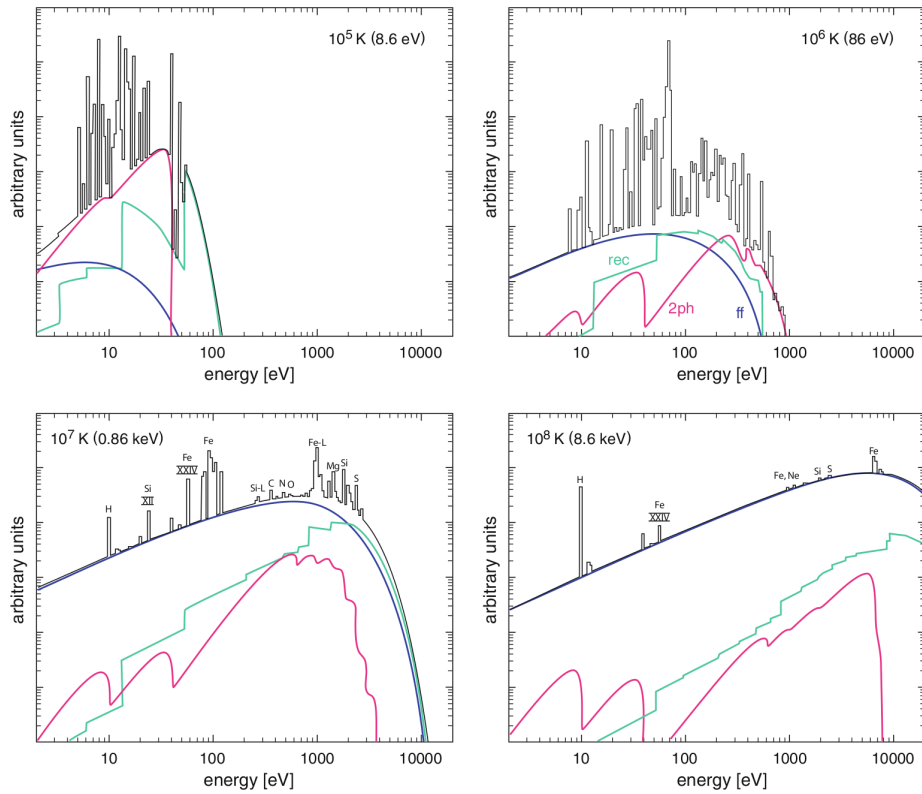


Figure 2.2: Examples of the X-ray spectra for solar abundances at different temperatures. The continuum components come from bremsstrahlung (blue), free-bound emission (green) and the two-photon radiation (red). (Böhringer and Werner, 2010)

Free-bound emission comes from the radiative recombination, when a free electron gets captured by an ion followed by the emission of a photon. Its spectrum is characterized by sharp ionisation edges.

The two-photon radiation concerns mostly the H- and He-like ions. The quantum mechanics forbids the radiative transition from 2s to 1s state, forcing the excited ion in most cases to wait for another collision, exciting it to the 2p state, from where it can return to the ground state through an allowed transition. However the tenuous ICM usually cannot provide another particle for the ion to collide with within a reasonable time. The decay from the 2s to 1s state then happens via emission of two photons, whose total energy is equal to the difference of the energy of the respective states.

Bremsstrahlung, as written before, is the dominant contributor to the ICM continuum emission. It arises from the free electron-ion collisions. We can express its emissivity – adopting the notation of Kaastra et al. (2008) – ϵ_{ff} (in photons $\text{m}^{-3} \text{s}^{-1} \text{J}^{-1}$) as

$$\epsilon_{\text{ff}} = \frac{2\sqrt{2}\alpha\sigma_T c n_e n_i Z_{\text{eff}}^2}{\sqrt{3\pi}E} \left(\frac{m_e c^2}{k_B T}\right)^{\frac{1}{2}} g_{\text{ff}} \exp\left(-\frac{E}{k_B T}\right), \quad (2.5)$$

with α the fine structure constant, σ_T the Thompson cross section, n_e and n_i the electron and ion densities respectively and E the energy of the emitted photon. The dimensionless quantity $g_{\text{ff}} \approx 1$ is called the Gaunt factor. We further need to define the effective charge of the ion Z_{eff} as

$$Z_{\text{eff}} = \sqrt{\frac{n_r^2 I_r}{E_H}}, \quad (2.6)$$

with E_H the ionisation energy of hydrogen, I_r the ionisation potential of the ion after a recombination and n_r the corresponding principal quantum number.

2.2.2 Line Emission

There are two basic steps in the process of the line radiation – the excitation of an ion and the emission itself.

Excitation can come around via various processes. The collisional excitation usually plays the most important role here, especially in plasmas in CIE. Alternatively an ion can get excited by absorbing a photon of given energy (although in ICM we neglect this, especially in the cluster outskirts), by a collision with a free electron, by photoelectric effect or finally the excitation can happen by capturing a free electron into one of the free energy levels above the ground state.

Whatever the excitation process, an electron can decay back to the ground state via emitting a photon of the energy equal to the energy difference between the respective states. We can express the total power line power P_{ij} (in photons per unit time per unit volume) as

$$P_{ij} = A_{ij} n_j, \quad (2.7)$$

2.3. HISTORICAL REMARKS

where A_{ij} is the transition probability (in s^{-1}) and n_j the number density of the ions excited to the state j . One has to solve a set of equations for all the energy levels of a given ion, taking into account all the relevant population and depopulation processes.

The quantum mechanics selection rules tell us which lines are allowed (described in e.g. Mewe (1999)). Higher-order processes sometimes allow the forbidden lines to occur. If there is no other quick enough way for an excited state j to decay, these lines can become quite strong, their power depending virtually only on the rate at which the ion is brought to the state j . This is precisely what happens in the ICM owing to its low density.

2.2.3 Physical Properties From the ICM X-ray Spectrum

Physical properties of the ICM are determined by fitting hot, thin plasma models to its observed spectrum. Currently the two most widely used thin plasma codes are MEKAL (Mewe et al., 1985, 1986; Kaastra and Mewe, 1992; Liedahl et al., 1995) and APEC (Smith et al., 2001), available in the majority of the X-ray fitting programs.

The main differences between the two are their line libraries and the way they deal with the physics, however they provide consistent results. Their differences can be used to study the robustness of the results.

It is generally advised to prefer APEC code over MEKAL when using the XSPEC fitting package (Arnaud, 1996), as the version of MEKAL included is obsolete. The latest version is then included in the SPEX fitting package (Kaastra et al., 1996).

2.3 Historical Remarks

The idea of the galaxy clusters containing diffuse gas was discussed for the first time by Limber (1959). Despite the lack of observational evidence he argues that the galaxy formation from parental clouds of gas cannot be completely efficient and also that galaxy collisions must occur in the denser cluster environment, ejecting interstellar gas out from the galaxies. Felten and Morrison (1966) discussed the spectral properties of “*relativistic electrons in tenuous regions of space*”.

With the dawn of the X-ray astronomy in the late 60’s the first detections of the ICM emission appeared. Byram et al. (1966) detected the central galaxy of the Virgo cluster – M87. The first observation of the extended X-ray emission of the Coma cluster was parallelly done by Meekins et al. (1971) using the *Aerobee 150* sounding rocket and Gursky et al. (1971) using the *Uhuru* satellite data. Combining these findings with the first *Uhuru* catalogue (Giacconi et al., 1972) enabled Gursky et al. (1972) to suggest that the majority of the galaxy clusters contain an extended X-ray source and have net luminosity of $10^{43} - 10^{44} \text{ erg s}^{-1}$. Solinger and Tucker (1972) used the observed relation between the X-ray luminosity L_X of clusters and the velocity dispersion of its galaxies to

2.3. HISTORICAL REMARKS

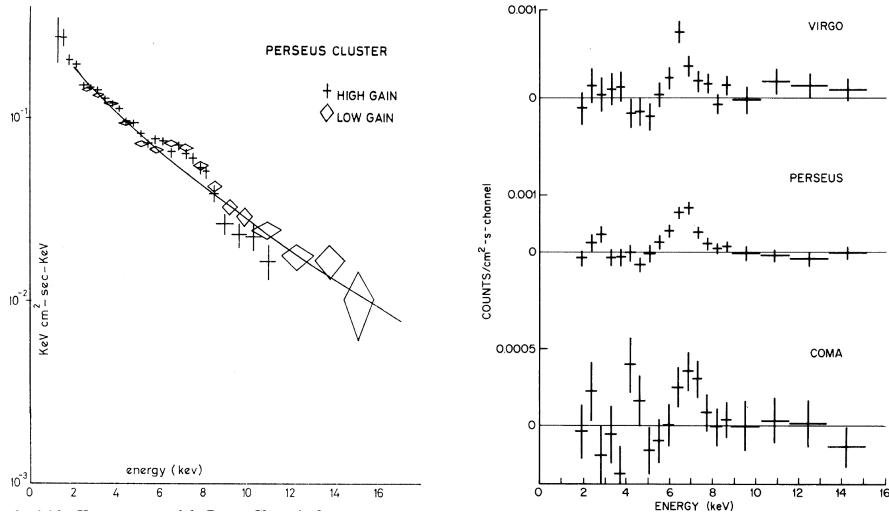


Figure 2.3: *Left:* The *Ariel 5* spectrum of the Perseus cluster. The solid line is the fitted adiabatic gas sphere model. The emission feature is clearly visible at ~ 7 keV. (Mitchell et al., 1976) *Right:* Residual counts from the respective clusters after subtracting the best-fit thermal model. (Serlemitsos et al., 1977)

investigate the source of the X-ray emission, which they describe by thermal-bremsstrahlung model. Further support for the bremsstrahlung was offered by the balloon-borne experiment by Scheepmaker et al. (1976). The observations in high energies ($\sim 20 - 150$ keV) resulted in no positive detection pointing to the presence of the steepening of the spectral slope present in the bremsstrahlung spectrum but not in the power-law.

The discovery of metals pollution in the ICM came with the observations of the Perseus cluster with the *Ariel 5* rocket (Mitchell et al., 1976), who have observed the Fe-K emission. Serlemitsos et al. (1977), using *OSO-8* data, confirmed their result and added the emission line evidence in the Virgo and Coma clusters. Their spectra are shown in Fig. 2.3. These observations also provided the final arguments for thermal origin of the emission as opposed to inverse Compton which was being discussed as well.

Once the true nature of the ICM was discovered the research (along with the instrumentation) turned to the spatial-resolved imaging and spectroscopy. First irregularities from the spherical symmetry of the ICM clouds were discovered (Wolff et al., 1974). The variability of the ICM properties in different parts of the clusters is the topic of the next chapter.

3

ICM Across the Cluster Volume

We devote this chapter to the discussion of the properties of the ICM change within the volume of the clusters. In Sect. 3.1 we will see that the ICM is not homogeneous and that we can divide the clusters into several categories based on the behavior of the ICM.

In Sec. 3.2 we summarize our (as of now sparse) observational knowledge of the outermost parts of the galaxy clusters. At the end of the chapter we briefly discuss the observatory *XMM-Newton* (cf. Sec. 3.3). This chapter does not include any section devoted solely to history because all the relevant results are mentioned in the text itself.

3.1 ICM in the Galaxy Clusters

Given the breathtaking size of the galaxy clusters, it is hardly surprising that the properties of the ICM change across their volume. Just a simple observation of the varying X-ray surface brightness of the ICM in a given cluster can offer a very strong suggestion of this.

It has been an ongoing effort to make a localized spectroscopy of the ICM since its discovery. However the properties of the first X-ray observatories did not allow for this – the instruments had either too little spatial or spectral resolution. Briel and Henry (1994) and Henry and Briel (1995) used *ROSAT* to create 2D temperature maps, however their errors were unreasonably large. The results of further papers were dependent on the method the authors used for the analysis and thus did not

Localized spectroscopy is of significant interest – it allows us to directly study the properties of the ICM at smaller-than-whole-cluster scales. However, it can be also used as a probe to the cluster mass. Assuming the hydrostatic equilibrium in the ICM and approximate spherical symmetry of the cluster one can write for the mass within the radius r

$$M(r) = -\frac{Gk_B T(r)}{\mu m_p} r \left(\frac{\log \rho_g}{\log r} + \frac{\log T(r)}{\log r} \right), \quad (3.1)$$

where G and k_B are the Newton's and the Boltzmann's constants respectively,

3.1. ICM IN THE GALAXY CLUSTERS

μ is the mean particle mass, m_p the proton mass and ρ_g the gas density. This relation can be derived by rewriting the condition of hydrostatic equilibrium under spherical symmetry, Eqn. 3.8.

The physical properties of the ICM do not remain constant over the cluster volume. In the first approximation we can assume isotropic variation in the ICM properties, centered on the bright central galaxy (BCG) changing only with the radial distance. This approximation works the better the older – and more relaxed – a given cluster is.

The basic properties which we use to describe the ICM (cf. Chap. 2) are the temperature, metallicity (or chemical composition in general) and the density. As described in the previous chapter, the first two are inferred from the spectroscopy.

As written before there is no spectroscopic tool to measure the density. Its value is determined from the fact that the surface brightness density of the bremsstrahlung continuum is proportional to the square of the density. This can be seen by writing down the expression for the collision rates R between the electrons and the ions that give rise to the bremsstrahlung radiation

$$R = n_e n_I C_{Ix} = n_e^2 \left[\frac{n_I}{n_E} \right] \left[\frac{n_E}{n_H} \right] \left[\frac{n_H}{n_e} \right] C_{Ix}(T), \quad (3.2)$$

where C_{Ix} are the collision rates coefficients for ion I , n_E , n_I and n_H are number densities respectively of the elements, ions and the hydrogen nuclei. In the square brackets the fractional abundances of various particle species appear.

While the galaxy clusters come in many sizes, by using the correct scaling we can discover self-similar behavior of the variations in the ICM properties. We therefore usually measure the distances from the cluster center in r_Δ , where Δ is the ratio of the mean density of the enclosed mass to the critical density of the Universe at given redshift, $\rho_{\text{crit}} = 3H^2/8\pi G$, where H is the Hubble and G the Newton constant respectively. It's current value is about one hydrogen atom per cubic meter. With the definition it's good to note that the value of Δ decreases as one moves out from the cluster center.

We define a so-called virial radius as the radius within which the matter is virialized, or equivalently has reached the hydrostatic equilibrium. It can be shown (Tozzi and Norman, 2001; Voit, 2005) that at the present epoch the virial radius is approximately equal to r_{180} . However due to the limited spatial resolution the value usually adopted is r_{200} .

ICM is optically thin, allowing us to see all the way to the cluster center (as opposed to for example stars, whose observed emission comes from the thin atmosphere on the surface). As we move from the outskirts towards the center we measure mixed spectrum from all the radii in our line of sight. We can then speak of two sets of the measured ICM profiles – projected (obtained from the modelling of the directly observed spectra) and deprojected (modelled after the subtraction of the effect of the outer layers). While the former are easier to measure and sufficient to draw some conclusions about the cluster in question, we use the latter when determining the density, entropy and pressure of the

ICM. The process of deprojection itself requires certain assumptions about the geometry of the ICM distribution (usually spherical symmetry) and good photon statistics and angular resolution.

3.1.1 Temperature of the ICM

Temperature of the ICM is usually determined from the shape of the bremsstrahlung emission (other methods, involving using various spectral lines are employed when one uses the high-resolution spectra, for details of some of these methods refer to Matsushita et al. (2002)).

Even before the possibility of localized ICM studies the temperature was used as a reliable proxy for the total cluster mass (including the dark matter) determination. If we assume a self-similar shape of the gravitational potentials then we can find from the virial theorem

$$T \propto \sigma_{DM}^2 \propto M/R \propto M^{2/3}, \quad (3.3)$$

where T is called *virial temperature*, σ_{DM}^2 is the dispersion of the velocity of the dark matter particles. Last relation comes from $M \propto R^3$ and the assumption of the constant density of the dark matter cloud. One finds the tightest relation between the temperature and the mass when using the data in the region $r = (0.15 - 1) \times r_{500}$ (Pratt et al., 2009), the reason being the presence of the cool cores.

The theory of the cooling flows was developed before it could have been observationally verified (see Fabian (1994) for review). The basic idea is that the emission of the radiation presents energy loss for the ICM. The emission rate is dependent on the square of the density, thus the denser the gas the faster it cools. The density of the ICM rises towards the cluster centers making the cooling time shorter. We can then find cooling radius r_{cool} inside which the cooling time is shorter than the age of the cluster. We can then expect to find a decreasing temperature profile in the cluster centers, thus the name cool core. Further consequence of this process would be the decrease of the pressure that would result in the outer ICM falling to the cluster center in what is called the cooling flow.

De Grandi and Molendi (2002) used *BeppoSAX* data to observe these decreasing temperature profiles for the first time. With the help of *XMM-Newton* and *Chandra* this picture has become even clearer.

Peterson et al. (2001) used the RGS on board of the *XMM-Newton* to study Abell 1835, finding inconsistencies with the cooling flow model when they failed to observe the expected temperature structure in the cluster center. Further detailed work (e.g. Fabian et al. (2005)) found the evidence of the strong interaction of the central AGN with the surrounding gas, which is now believed to be the source of heating, posing another complication to the cooling flow model.

In Fig. 3.1 we can see the temperature profiles of 15 nearby ($z < 0.2$) *XMM-Newton* clusters analyzed by Pratt et al. (2007). Outside r_{cool} they behave in

the self-similar way with the temperature decreasing. We can also distinguish cool core (CC) and non-cool core (NCC) clusters.

One of the most important goals of the present-day X-ray research of the galaxy clusters is the explanation of the self-similar behavior of the profiles and also the scatter around the mean.

3.1.2 Metallicity of the ICM

Due to their deep gravitational potential wells the galaxy clusters retain all the metals produced by their stellar populations and thus help us study the chemical evolution of the Universe.

Dominant fraction of these elements resides in the ICM. Due to the optical thinness and the relative simplicity in the physical description of the environment the abundances obtained from the ICM observations are more robust than those from other sources (stellar populations, H II regions; for general review see Werner et al. (2008a)).

The majority of the elements from O up to Fe are being produced in supernovae, that can be roughly divided into type Ia supernovae (SN Ia; most probably the results of the thermonuclear explosions of accreting white dwarves) and the core collapse supernovae (SN_{CC}). The former produce large amounts of Fe, Ni and Si- group elements while at the same time only a little of O, Ne and Mg. Combining the models of the various supernova element yields with the initial mass function (IMF) of the cluster stellar population allows us to interpret the observed high resolution spectra of the ICM and study the supernova enrichment history of the ICM. The emergent picture these days is the initial homogeneous enrichment by the SN_{CC} followed by SN Ia exploding prominently in the BCG (see Finoguenov et al. (2000) for the first such observation with *ASCA*).

The origin of the C and N elements still remain a matter of debate. It is believed that in general a large amount of sources contribute, one of them being the winds of low- and intermediate mass asymmetric giant branch stars (Werner et al., 2006).

There is a difference in the metallicity profiles of CC and NCC clusters. De Grandi and Molendi (2001) used *BeppoSAX* observations of 17 nearby clusters to find that while NCC clusters tend to have flat metallicity profiles, metallicity¹ is enhanced towards the centers in the CC ones. These results have been confirmed by the *XMM-Newton* and *Chandra* (Vikhlinin et al., 2005; Pratt et al., 2007).

The metallicity measurement can get affected by various biases, this especially happens when the underlying temperature structure is incorrectly modelled. Fitting a multi-temperature plasma spectrum with a one-temperature model results in low value of metallicity. The underlying multi-temperature structure can give rise to the emission of the same lines of various ionisation states of the element and thus of slightly different energies. As demonstrated

¹Alternatively we can use the term Fe abundance. Since the metallicity is usually expressed as a fraction of solar chemical composition using the Fe lines, these terms can often be used as synonyms.

3.1. ICM IN THE GALAXY CLUSTERS

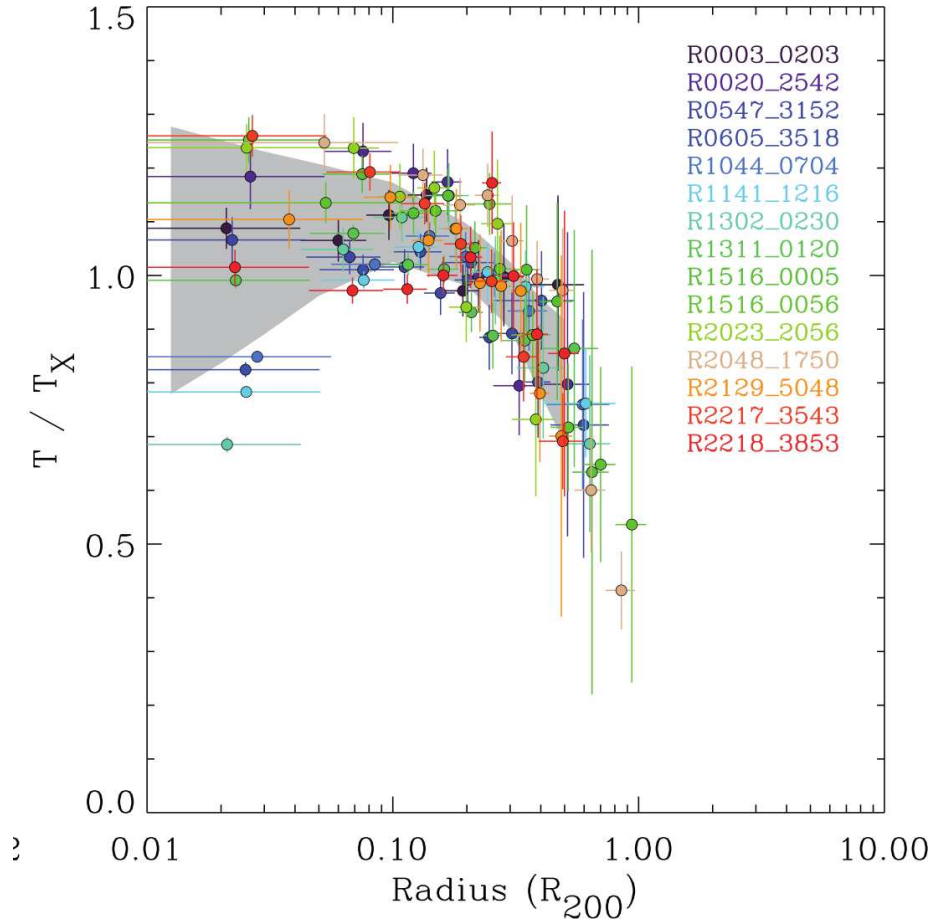


Figure 3.1: Temperature profiles for 15 *XMM-Newton* clusters. The x-axis is scaled in the r_{200} units, y-axis shows the logarithmic temperature normalized by mean spectroscopic temperature in $0.1 - 0.4 r_{200}$. The grey area shows the mean plus minus 1σ standard deviation. (Pratt et al., 2007)

by Buote (2000b), fitting a one temperature model to a low (~ 1 keV) multi-temperature plasma will result in the model to increase the continuum and lower the metallicity due to the wider than expected appearance of the Fe L complex. The lack of proper modeling of the temperature structure can then result in observing a downward turn of the metallicity as one moves towards the core of a CC cluster, where the structure of the plasma is more complicated.

3.1.3 Properties Obtained by Deprojection

In this subsection we discuss the ICM properties that we infer from the deprojection of the cluster spectra. These are the density, pressure and entropy.

The density is tightly bound with the surface brightness. As mentioned before there is no direct spectral feature that would allow us to infer the gas density and we need to use the surface brightness.

A number of theoretical models have been developed to describe how the density varies with the cluster radius. Numerical simulations by Navarro et al. (1997) show that the dark matter cloud density should follow power-law in the outskirts and a flatter power-law in the center. It can be described by the NFW profile

$$\rho_{\text{DM}} = \rho_s \left[\left(\frac{r}{r_s} \right) \left(1 + \frac{r}{r_s} \right)^2 \right]^{-1}, \quad (3.4)$$

where ρ_s and r_s are the scaling density and radius respectively.

Previously however alternative models were used, one of them being the constant density core function

$$\rho_{\text{DM}} = \rho_{\text{DM},0} \left[1 + \left(\frac{r}{r_c} \right)^2 \right]^{-3/2}, \quad (3.5)$$

with $\rho_{\text{DM},0}$ and r_c the central density and core radius respectively. Assuming this function to describe the total matter density or assuming isotropic gaussian velocity distribution of the galaxies, the gas density can be described by the *beta model*

$$\rho(r) = \rho_0 \left[1 + \left(\frac{r}{r_c} \right)^2 \right]^{-3\beta/2}. \quad (3.6)$$

For isothermal gas the surface brightness then follows the relation

$$I_X(r) = I_X^0 \left[1 + \left(\frac{r}{r_c} \right)^2 \right]^{-3\beta+1/2} \quad (3.7)$$

While this model with $\beta \approx 2/3$ gives reasonable fit in the outer parts of the clusters, it tends to underestimate the surface brightness in the cluster centers (Jones and Forman, 1984).

3.2. OBSERVING THE ICM OUT TO THE VIRIAL RADIUS

Pressure in the hydrostatic equilibrium balances the gravity

$$\nabla P = -\rho \nabla \Phi, \quad \frac{1}{\rho} \frac{dP}{dr} = -\frac{GM(r)}{r^2}, \quad (3.8)$$

where $M(r)$ is the total cluster mass inside r . The second equation assumes the spherical symmetry. Since this is one equation for two variables we also need to provide the entropy distribution to fully describe the gas. Using the spectroscopic results we calculate the pressure simply as $P = n_e kT$.

Observing the pressure profile one can discover a number of interesting features in the ICM, most prominently shock fronts and the cold fronts.

Entropy is one of the fundamental properties of the ICM determining its structure and recording the history. Simply speaking, the high entropy gas floats while the low entropy one sinks, resulting in convection within the ICM until the isoentropic surfaces coincide with the equipotential surfaces. The entropy as a thermodynamic quantity remains constant throughout the adiabatic processes in the gas, therefore unexpected behavior of the entropy suggests generally speaking an interesting process in the cluster's past (alternatively it can also point to a bias in the modeling as we will see in Subs. 4.3.1).

Modeling the ICM as ideal gas, the specific entropy (entropy per particle) is given by

$$s = \frac{3}{2} k \ln \left(\frac{P}{\rho^{5/3}} \right) = \frac{3}{2} k \ln \left(\frac{T}{\rho^{2/3}} \right). \quad (3.9)$$

However, more often we use the so-called entropy parameter K

$$K = \frac{kT}{n_e^{2/3}}, \quad (3.10)$$

defined to avoid the logarithmic structure of the entropy with the unit keV cm². We see that $s \propto \ln K$. Numerical models by Tozzi and Norman (2001) predict for a cluster formed by the process of the smooth accretion the entropy to follow the power-law profile $K(r) \propto r^{1.1}$.

3.2 Observing the ICM Out to the Virial Radius

Studying of the galaxy clusters has been an ongoing effort for decades, however the major sources of information have either come from the computer simulations or the observations of the central parts of the clusters (within $r_{500} \approx 0.5 r_{200}$ or even less) – to this day we have only a handful of the cluster outskirts observations. This is due to the low surface brightness of the ICM in the cluster outskirts. The emission gets lost in the X-ray fore- and background².

What we are left with is the observational knowledge of the central parts that comprise only a small fraction of the whole cluster volume as well as the cluster

²We are not using the simple term background here because a significant part of the observed X-ray radiation originates within our own Galaxy, i.e. in the foreground

3.2. OBSERVING THE ICM OUT TO THE VIRIAL RADIUS

mass. For the sake of the further modelling of for example the mass profiles we turn to extrapolations, which is far from ideal since the conclusions are not based on observations. Worth mentioning is also the fact that according to the present models the clusters form by accreting the gas from the mass filaments of the cosmic web. By observing the outskirts we could then be able to study this process in real time and see the large scale structure of the universe form in real time.

X-ray photometry of the cluster outskirts does not require the photon statistics as good as the spectroscopy and therefore precedes the spectroscopic results in the field. Vikhlinin et al. (1999) use a sample of 39 galaxy clusters from *ROSAT* to study the shape of the cluster X-ray brightness profiles in the outskirts using the data from $0.3 r_{200}$ to (and beyond) the virial radius. They find a weak correlation between the shape of the surface brightness and the cluster temperature but confirm the theoretical result of the tight relation between the radius and temperature of the cluster. Neumann (2005) stack the brightness profiles of the clusters with similar temperature to enhance the statistics, using a sample of 14 *ROSAT* clusters.

Spectroscopy of the ICM in the cluster outskirts requires a much better photon statistics as well as careful modelling of both the detector noise and the cosmic X-ray fore- and background (CXFB). Therefore until recently only the *Suzaku* satellite was capable of providing data of the sufficient quality. Its orbit lies inside the Van Allen radiation belts that protect it from the solar wind particles and results in an exceptionally low instrumental background. The analysis of the first *XMM-Newton* observation of this kind is the main goal of this thesis and is described and discussed in Chap. 4.

At the time of writing the properties of the ICM of only a handful of clusters have been described out to the virial radius based on the observations. In the chronological order these are PKS 0745-191 (George et al., 2009), Abell 2204 (Reiprich et al., 2009), Abell 1795 (Bautz et al., 2009), Abell 1413 (Hoshino et al., 2010) and the Perseus cluster (Simionescu et al., 2011). The last one mentioned is the most detailed, showing that the ICM in the cluster outskirts is highly clumped and also is the only to include the metallicity measurement of the cluster's ICM. All the mentioned clusters are old and relaxed with virial radii at over 1.5 Mpc.

Studying the chemical composition in the cluster outskirts has eluded the observers for the longest time and still remains one of the most challenging tasks. Fujita et al. (2008) were the first ones to obtain reasonable results; using the *Suzaku* observation of the link region between Abell 399 and Abell 401 they determined the metallicity to be $\sim 0.3 Z_{\odot}$, comparable to that in the central regions. They conclude that the metallicity is fairly homogeneous within the virial radius. Simionescu et al. (2011) measure the metallicity at the virial radius of the Perseus cluster to be $\sim 0.3 Z_{\odot}$.



Figure 3.2: Artist's impression of *XMM-Newton*. Image courtesy of ESA.

3.3 XMM-Newton

The data we analyzed in this thesis were obtained by ESA's X-ray observatory *X-ray Multi-Mirror Mission (XMM-Newton)*. In this section we briefly describe the basic properties of the satellite.

Launched on 10th December 1999, the *XMM-Newton* is the second cornerstone in ESA's Horizon 2000 programme. Fig. 3.2 shows the artist's impression of the satellite. Three Wolter type-1 X-ray telescopes are clearly visible as well as the rear part containing all the scientific instruments.

XMM-Newton carries a total of six instruments aboard. Three CCD cameras, MOS 1 (metal oxide semiconductor), MOS 2 and pn, collectively assembled into European Photon Imaging Camera (EPIC), are used for X-ray imaging and moderate resolution spectroscopy. Two identical X-ray spectrometers are the essential parts to the Reflective Grating Spectrometer (RGS), an instrument used for high-resolution spectroscopy. The Optical Monitor (OM) extends the range of electromagnetic spectrum visible to the observatory by optical/UV, enabling it to simultaneously gather data in all the mentioned bands.

XMM-Newton is placed into a highly elliptical orbit. This allows for high continuous target visibilities for up to 40 hours.

In our analysis we were using only the EPIC data. The camera is sensitive in soft X-rays (0.15 – 12.0 keV for MOSes, 0.15 – 15.0 keV for pn). Each of the

3.3. XMM-NEWTON

instruments has the field of view of $\sim 30'$ with a good angular resolution. The point-spread function (PSF) has the full width at half maximum (FWHM) of $5''$ for MOS and $6''$ for pn. The CCDs also offer a moderate spectral resolution of about $E/\Delta E \approx 20 - 50$ ³.

During its lifetime of currently more than a decade *XMM-Newton* has been helpful in unveiling many secrets of the Universe, ranging from the black holes to the origins of the Universe itself. Statistically speaking at the time of writing (spring 2011) there is over 1.3 refereed papers per one *XMM-Newton*'s revolution.

Further details about the spacecraft itself, the data analysis or the manual for the proposers can be found at *XMM-Newton*'s website <http://xmm.esac.esa.int/>.

³ $E/\Delta E$ of the RGS is about a magnitude higher, however the instrument is not suitable for exploring the extended sources such as the galaxy clusters in our case.

4

Virgo Cluster Out to the Virial Radius

In this chapter we describe the results of the analysis of the *XMM-Newton* data of the Virgo cluster. All the results, discussions and figures come from Urban et al. (2011).

4.1 Observations and Data Reduction

We analyzed a total of 14 *XMM-Newton* pointings, details of which are given in Tab. 4.1. All of the observations were archival, majority conducted in June and July 2002 with the exception of the southernmost ones. The pointings are partially overlapping, covering a stripe of the sky with the dimensions roughly 4.5° (North-South direction) by $30'$ (East-West). The mosaic of our data is shown in Fig. 4.1. The northernmost pointing (not in the figure), located 5.5° to the north of the cluster center was assumed not to contain any cluster emission and we used it to model the local X-ray background.

4.1.1 Data Analysis

We used *XMM-Newton* Science Analysis System (SAS) version 9.0.0 to process the data. The filtering and the data product extraction from the MOS detectors were performed using the *XMM-Newton* Extended Source Analysis Software (XMM-ESAS) as described in Kuntz and Snowden (2008); Snowden et al. (2008); Snowden and Knutz (2010). For the analysis of the pn data the methods described in Werner et al. (2008b) were used. Detailed technical description of the process can be found in Urban et al. (2011) and the papers referred therein.

The observations 0106060701 and 0106061101 were found to be strongly affected by the flares and were not used in the subsequent analysis. The data from pn of the observation 0106060201 also showed strong indication of residual soft-proton contamination and were not used further.

Table 4.1: Summary of the observations. Columns give the observation identifier, starting date of the observation, *XMM-Newton* revolution of the observation, total and cleaned exposure times for MOS1, MOS2 and pn instruments respectively, and the coordinates of the pointings. The pointings in the table are ordered from the south to the north.

obs. ID	date DD/MM/YY	rev.	Exp. time [ks]			Clean time [ks]			RA [°]	DEC [°]
			MOS1	MOS2	pn	MOS 1	MOS 2	pn		
0200920101	11/01/05	932	95.36	95.37	– ^(a)	74.87	75.65	–	187.71	12.36
0106060101	12/07/01	291	9.28	9.28	5	8.75	9.04	5	187.71	12.73
0106060201	08/07/02	472	8.36	8.37	5	4.65	4.51	1.7	187.71	13.06
0106060301	04/07/02	470	8.89	8.89	5.52	6.87	7.3	5.1	187.71	13.39
0106060401	04/02/02	470	11.33	11.35	7.64	10.54	10.68	6.77	187.71	13.73
0106060501	06/07/02	471	17.38	17.42	13.87	14.3	14.7	11.58	187.71	14.06
0106060601	08/07/02	472	14.37	14.37	11	9.38	9.81	8.52	187.71	14.39
0106060701	05/07/02	471	13.85	13.87	10.5	4.89	6.09	0	187.71	14.73
0106061401 ^(b)	13/06/02	460	8.23	8.26	4.88	7.84	7.92	4.88	187.71	15.06
0106060901	10/06/02	458	15.03	15.03	11	11.28	11.38	7.8	187.71	15.39
0106061001	06/06/02	456	12.39	12.18	8.89	8.58	8.45	5	187.71	15.73
0106061101	09/06/02	458	15.93	15.95	11.98	8.31	8.43	4.96	187.71	16.06
0106061201	09/06/02	458	17.57	17.65	13.52	14.19	14.36	10.22	187.71	16.39
0106061301 ^(c)	10/06/02	458	15.99	16.03	12	14.7	14.39	11.33	187.71	17.89

^(a) data from pn were not used for the central pointing

^(b) replacement for flared observation 0106060801

^(c) background pointing (see text)

4.1. OBSERVATIONS AND DATA REDUCTION

The images for the surface brightness profile construction were extracted in the 0.6 – 3.0 keV energy range. The images from all three detectors were stacked and we employed the SAS task `EWAVELET` to identify the point sources down to 5σ significance. Subsequently the images were visually checked for false detections, sources with larger dimension and those that were missed by `EWAVELET`. For the central pointing the list of sources from Simionescu et al. (2010) was used.

In order to minimize the systematic errors from large off-axis measurements (e.g. effective area calibration uncertainties) we used only the central $12'$ of each pointing, centered on the individual aim points for each detector respectively.

4.1.2 Spectral Analysis

All the observations north of the central pointing were used for the extraction of the spectrum. The central region of Virgo has been extensively studied by e.g. Belsole et al. (2001); Böhringer et al. (2001); Molendi (2002); Matsushita et al. (2002, 2003); Werner et al. (2006); Simionescu et al. (2007, 2008, 2010).

We extracted spectra from a series of annular regions centered on the galaxy M87, the Virgo cluster's BCG ($\alpha = 12^{\text{h}}30^{\text{m}}49.4^{\text{s}}$, $\delta = 12^{\circ}23'38''$). Their width varied to keep roughly the same number of the background-subtracted counts (10000) in each region. Spectral response files were created for each spectrum using the SAS tasks `RMFGEN` and `ARFGEN`.

`XSPEC 12.6.0` (Arnaud, 1996) was used to model the spectra. We used the 0.4 – 7.0 keV energy interval for modelling leaving out the 1.2 – 1.8 keV region to exclude the instrumental Al and Si lines. The ICM emission was modeled using the one-temperature `apec` model (Smith et al., 2001) for optically thin plasma in collisional ionisation equilibrium. We kept the redshift constant ($z = 4.36 \times 10^{-3}$) at the value of the BCG. The galactic absorption column was estimated based on the Leiden/Argentine/Bonn Survey (Kalberla et al., 2005) and the metallicities reported are relative to those by Grevesse and Sauval (1998). We used the extended C-statistics (allowing for the background subtraction) in all the regions.

As written before we extracted the cosmic X-ray foreground/background spectrum (CXFB) from the northernmost pointing (not shown in Fig. 4.1). After removing all the point sources we assumed three components of the CXFB spectrum – an absorbed power-law due to the unresolved point sources (De Luca and Molendi, 2004), the Galactic halo emission with the temperature of ~ 0.2 keV (Kuntz and Snowden, 2000) and the emission from the Local Hot Bubble modelled as 0.08 keV thermal plasma (Sidher et al., 1996; Kuntz and Snowden, 2000). The resulting CXFB parameters are summarized in Tab. 4.2.

4.1. OBSERVATIONS AND DATA REDUCTION

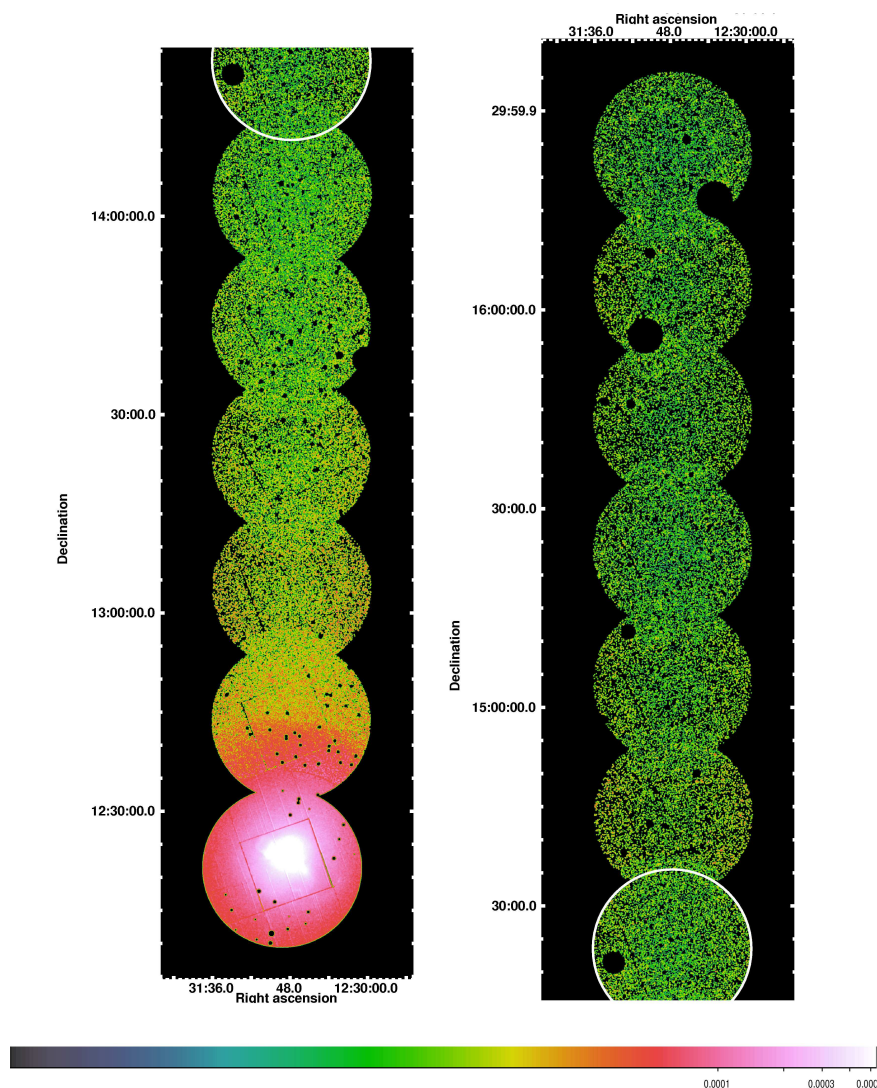


Figure 4.1: Mosaic *XMM-Newton* image in the 0.6 – 3.0 keV energy range. The background pointing lies 1.5° to the north of the northernmost pointing shown. Only the central region within the radius of $12'$ from the telescope's aim-point was used for each instrument. The image has been exposure-corrected, smoothed with a gaussian with the width of 3 pixels, and the point sources have been removed. The left panel shows the southern part of the mosaic and the right panel shows the northern part. The white circle marks the overlap in both panels. The central part of the cluster is clearly dominated by the emission of M87, the cold front discussed in Simionescu et al. (2010) is visible at $\sim 20'$ to the north of the center.

Table 4.2: Fore- and background model parameters. Fluxes are given in the 2–10 keV interval. The second column lists the photon index of the absorbed power-law component and the temperatures of the two foreground thermal components. GH stands for Galactic Halo, LHB for Local Hot Bubble.

component	Γ /Temperature [keV]	intensity [$\text{erg s}^{-1} \text{cm}^{-2} \text{deg}^{-2}$]
power-law	1.44 ± 0.03	$11.90^{+0.06}_{-0.07} \times 10^{-11}$
apec _{GH}	$0.191^{+0.005}_{-0.004}$	$(6.32 \pm 0.32) \times 10^{-16}$
apec _{LHB}	0.08^\dagger	$8.47^{+0.72}_{-0.64} \times 10^{-21}$
† fixed value		

4.2 Results

4.2.1 X-ray Surface Brightness

We present the X-ray surface brightness profile in Fig. 4.2. It was obtained from the background- and exposure-corrected MOS images in the 0.6–3.0 keV range. A total of 199 annular regions centered on M87 were used, covering the cluster out to ~ 255 arcmin which corresponds to ~ 1.2 Mpc projected distance. Out to ~ 8.5 arcmin = 40 kpc the regions are $0.1'$ wide, at the intermediate radii their width is ~ 1.35 arcmin and beyond 700 kpc they are binned to the width of $\sim 2.7'$. The reason for this is to smooth out the statistical fluctuations – the increasing bin-size keeps at least 500 counts in each bin, making the fluctuations in the cluster outskirts formally highly statistically significant. The gaps in the profile come from the unused flared observations.

The value of the background was assumed to be constant over the whole cluster, its value being the average surface brightness of the background region.

Apart from the already mentioned statistically significant fluctuations in the outskirts, the profile contains also a prominent feature at ~ 90 kpc which corresponds to the cold front discussed previously by Simionescu et al. (2010). The profile outside the cold front can be fitted with a power-law model $S_x \propto r^{-\alpha}$ with $\alpha = 1.34 \pm 0.01$ with no significant difference between the slopes of the profiles obtained from different low-energy intervals.

4.2.2 Spectral Results

The results of the spectral analysis are written in Tab. 4.3 and shown in Fig. 4.3. The cold front at ~ 90 kpc is apparent in both the temperature and metallicity as an obvious discontinuity. Described by Simionescu et al. (2010) and modelled by Roediger et al. (2011), this feature is the consequence of the gas sloshing in the Virgo cluster cooling core.

There is an abrupt drop in both the temperature and metallicity. At the

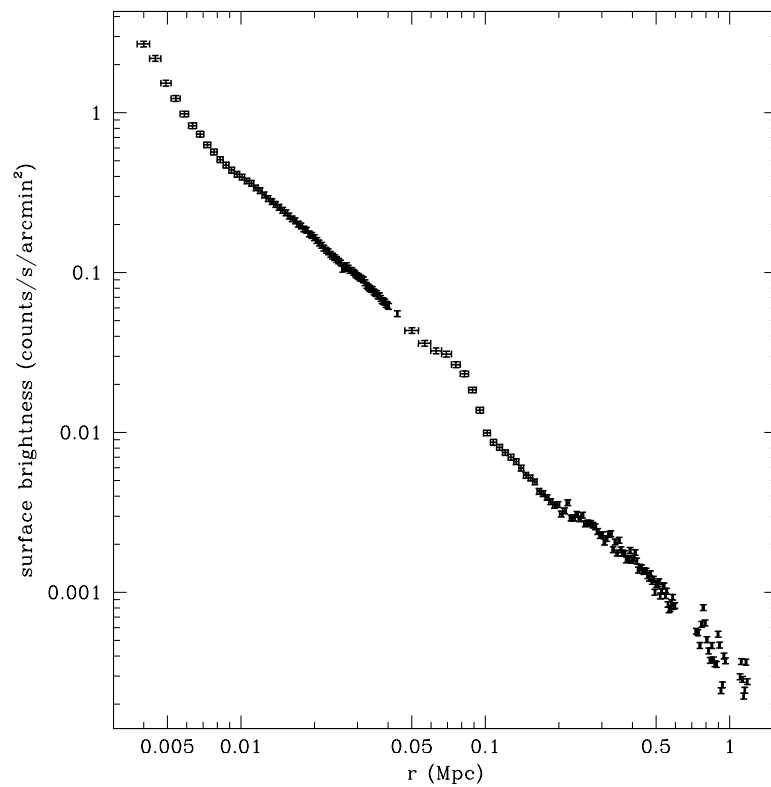


Figure 4.2: Background-subtracted surface brightness profile in the 0.6–3.0 keV band. The gaps in the profile indicate missing data due to flared observations. The virial radius, which we define as r_{200} , lies at about 1.08 Mpc.

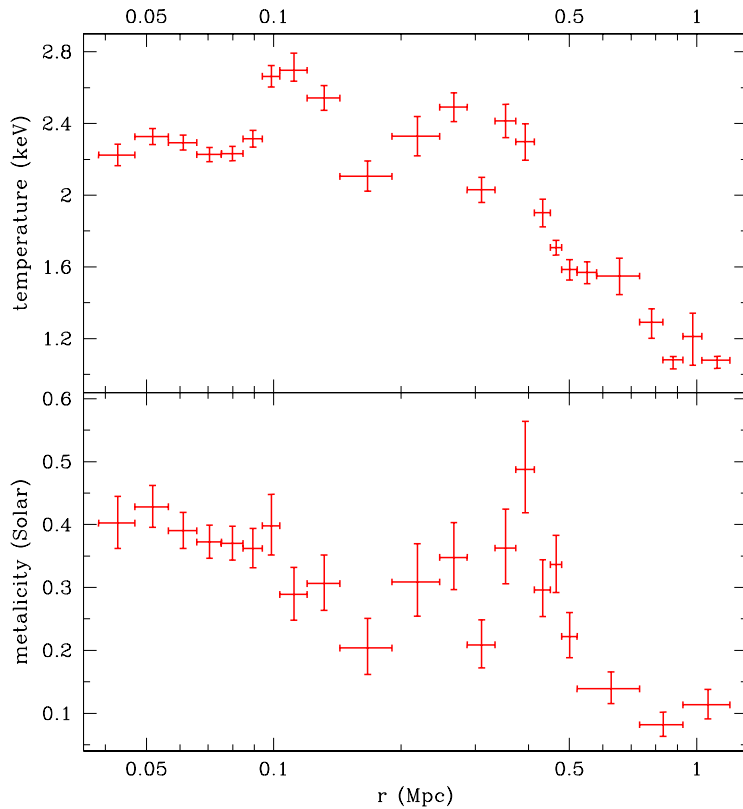


Figure 4.3: Projected temperature and metallicity profiles. The virial radius, which we define as r_{200} , lies at about 1.08 Mpc.

virial radius the properties reach the values of $kT = 1.08_{-0.05}^{+0.02}$ and $Z = 0.11 Z_{\odot}$ respectively. The metallicity has never been measured so significantly ($> 5.5\sigma$) before. This was made possible by the favorable conditions at the Virgo’s virial radius, namely the cluster’s proximity and ~ 1 keV temperature at the virial radius. At this temperature the Fe L emission peaks and *XMM-Newton* mirrors have large effective area, giving the optimal signal-to-detector background contrast.

This can clearly be seen at Fig. 4.5, where the spectra from two regions are shown, 522 – 580 kpc ($\sim 0.5 r_{200}$) and the outermost one at 1029 – 1198 kpc ($\sim r_{200}$) respectively. The over-plotted solid lines show the CXFB model, bottom panels show the ratio of the X-ray to the background flux. Near the virial radius the emission at 0.8 – 1.2 keV is really prominent and is associated with the emission of the Fe L complex.

To derive further properties we performed the deprojection of the set of the

4.2. RESULTS

Table 4.3: Projected temperatures, metallicities, and normalizations obtained from spectral fitting. The first and the second columns give the inner and outer radii of the annular extraction regions.

Radius [arcmin]		Temperature	Metallicity	Normalization
Inner	Outer	[keV]	[Solar]	$[1 \times 10^{-5} \text{ arcmin}^{-2}]$
8.2	10	$2.224^{+0.061}_{-0.060}$	$0.40^{+0.04}_{-0.04}$	$121.39^{+2.72}_{-2.73}$
10	12	$2.326^{+0.045}_{-0.045}$	$0.43^{+0.03}_{-0.03}$	$91.63^{+1.54}_{-1.54}$
12	14	$2.293^{+0.042}_{-0.041}$	$0.39^{+0.03}_{-0.03}$	$74.46^{+1.14}_{-1.13}$
14	16	$2.227^{+0.040}_{-0.039}$	$0.37^{+0.03}_{-0.03}$	$60.48^{+0.89}_{-0.88}$
16	18	$2.232^{+0.041}_{-0.040}$	$0.37^{+0.03}_{-0.03}$	$47.68^{+0.72}_{-0.72}$
18	20	$2.314^{+0.047}_{-0.047}$	$0.36^{+0.03}_{-0.03}$	$35.22^{+0.59}_{-0.59}$
20	22	$2.663^{+0.061}_{-0.061}$	$0.40^{+0.05}_{-0.05}$	$22.25^{+0.53}_{-0.52}$
22	25	$2.697^{+0.096}_{-0.060}$	$0.29^{+0.04}_{-0.04}$	$16.53^{+0.32}_{-0.32}$
25	30	$2.542^{+0.069}_{-0.068}$	$0.31^{+0.05}_{-0.04}$	$13.43^{+0.30}_{-0.30}$
30	40	$2.105^{+0.086}_{-0.083}$	$0.20^{+0.05}_{-0.04}$	$10.10^{+0.33}_{-0.33}$
40	52	$2.328^{+0.111}_{-0.109}$	$0.31^{+0.06}_{-0.05}$	$7.01^{+0.23}_{-0.23}$
52	61	$2.491^{+0.081}_{-0.080}$	$0.35^{+0.06}_{-0.05}$	$5.64^{+0.15}_{-0.15}$
61	71	$2.030^{+0.070}_{-0.070}$	$0.21^{+0.04}_{-0.04}$	$4.46^{+0.13}_{-0.13}$
71	79	$2.413^{+0.093}_{-0.093}$	$0.36^{+0.06}_{-0.06}$	$3.93^{+0.13}_{-0.12}$
79	88	$2.298^{+0.101}_{-0.102}$	$0.49^{+0.08}_{-0.07}$	$3.00^{+0.11}_{-0.11}$
88	96	$1.902^{+0.077}_{-0.078}$	$0.30^{+0.05}_{-0.04}$	$2.99^{+0.10}_{-0.10}$
96	102	$1.708^{+0.039}_{-0.042}$	$0.34^{+0.05}_{-0.04}$	$2.48^{+0.09}_{-0.09}$
102	111	$1.585^{+0.055}_{-0.058}$	$0.22^{+0.04}_{-0.03}$	$2.36^{+0.09}_{-0.09}$
111	123	$1.569^{+0.061}_{-0.062}$	$0.14^{+0.03}_{-0.02}$	$2.16^{+0.08}_{-0.07}$
123	156	$1.549^{+0.098}_{-0.103}$		$1.64^{+0.07}_{-0.07}$
156	177	$1.292^{+0.074}_{-0.090}$	$0.08^{+0.02}_{-0.02}$	$1.47^{+0.08}_{-0.07}$
177	197	$1.081^{+0.020}_{-0.050}$		$0.87^{+0.06}_{-0.06}$
197	219	$1.213^{+0.129}_{-0.161}$	$0.11^{+0.02}_{-0.02}$	$1.07^{+0.09}_{-0.09}$
219	255	$1.080^{+0.022}_{-0.045}$		$0.64^{+0.05}_{-0.05}$

spectra using the `PROJECT` model in `XSPEC`. To ensure the stability of the fit we linked some of the parameters in the neighboring regions. The derived electron density profile is shown in the top panel of Fig. 4.4. Outside the cold front it can be fitted with a power-law model $n_e \propto r^{-\beta}$ with $\beta = 1.21 \pm 0.12$.

Using the deprojected density and temperature we were able to construct the entropy ($K = kT/n_e^{2/3}$) and pressure ($P = n_e kT$) profiles, they are shown in the middle and the bottom panels of Fig. 4.4 respectively. We over-plot a power-law $K \propto r^{1.1}$ on the entropy profile, which is expected from the gravitationally collapsed gas in hydrostatic equilibrium (Tozzi and Norman, 2001; Voit, 2005). The ICM follows this profile out to ~ 450 kpc where it flattens out, staying consistently below the expected value by a factor of 2 – 2.5. This measurement is remarkable – its robustness implies that the temperature is underestimated and/or the density is higher.

A model by Arnaud et al. (2010) is over-plotted in the pressure profile. It is an average profile from a sample of clusters observed out to $\sim 0.5r_{\text{vir}}$ extrapolated to the larger radii. There are clear departures from the profile at ~ 200 kpc, ~ 400 kpc and ~ 600 kpc.

The unrelaxed nature of the Virgo cluster is the reason why the results of the deprojection assuming spherical symmetry should be treated with caution. Measurement errors are significantly smaller than the systematic errors arising from the departures from the spherical symmetry.

4.2.3 Systematic Errors

We tested the robustness of our results against several possible sources of systematic errors.

In Fig. 4.6 we plot the temperature profiles for the single EPIC instruments. While the MOS results are at remarkable agreement with each other, pn temperature tends to be systematically higher. The biggest difference occurs in the last-but-one region (indicated with the dashed line in Fig. 4.6). We were not able to find any reason for this big inconsistency, however the pn data for this region were not used in the spectral analysis. Generally speaking all the results are in relative agreement with each other and the temperature drop at large radii is robust.

The assumption of the single model of the CXFB over the whole observation was tested by varying the fitted components of the model one at a time. The variation of the soft foreground components was determined by studying the *ROSAT* All Sky Survey (RASS) maps in the soft (0.1 – 0.3 keV) band, where most of the soft foreground is emitted in. The LHB and Galactic Halo (GH) flux variation was set to a conservative limit of 30 per cent. *ROSAT* hardness ratio maps were used to determine the GH temperature variation to 20 per cent. Having excluded the point sources we assumed the variation in the power-law component normalisation to be smaller than the statistical uncertainty with which it had been fitted. We therefore varied this parameter by its 3σ statistical error.

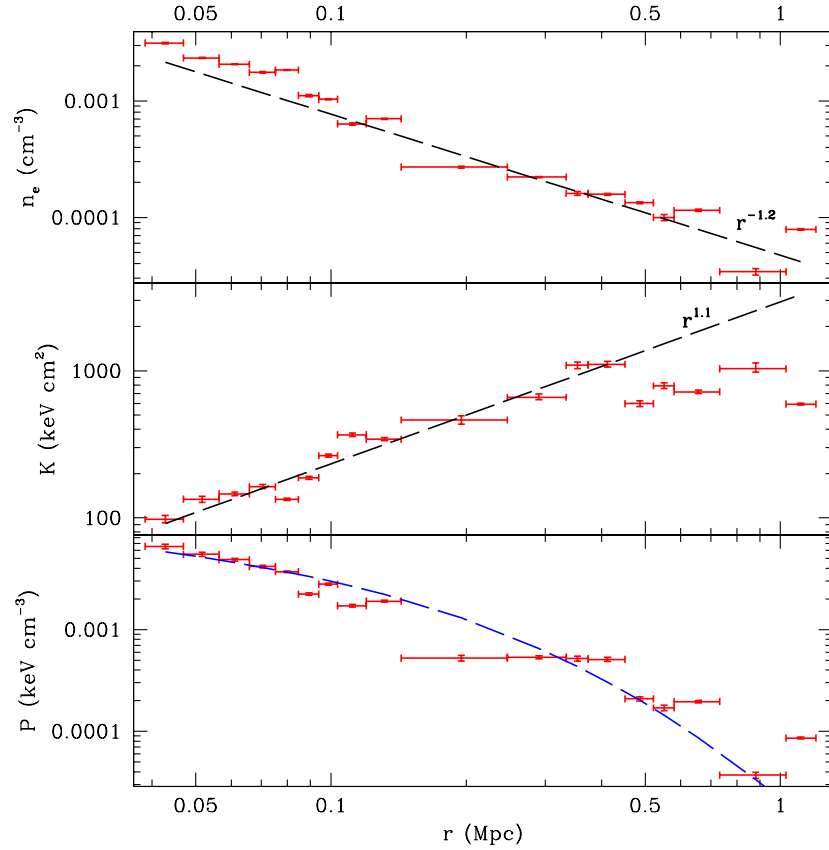


Figure 4.4: The deprojected electron density (n_e), entropy (K), and pressure (P) profiles. For the density profile, we overlay the best fit power-law model, $n_e \propto r^{-1.2}$. On the entropy profile we over-plot $K \propto r^{1.1}$, which is expected for gravitationally collapsed gas in hydrostatic equilibrium. On the pressure profile, we over-plot the extrapolated average profile determined for a sample of clusters within $\sim 0.5 r_{200}$ by Arnaud et al. (2010). The virial radius, which we define as r_{200} , lies at about 1.08 Mpc.

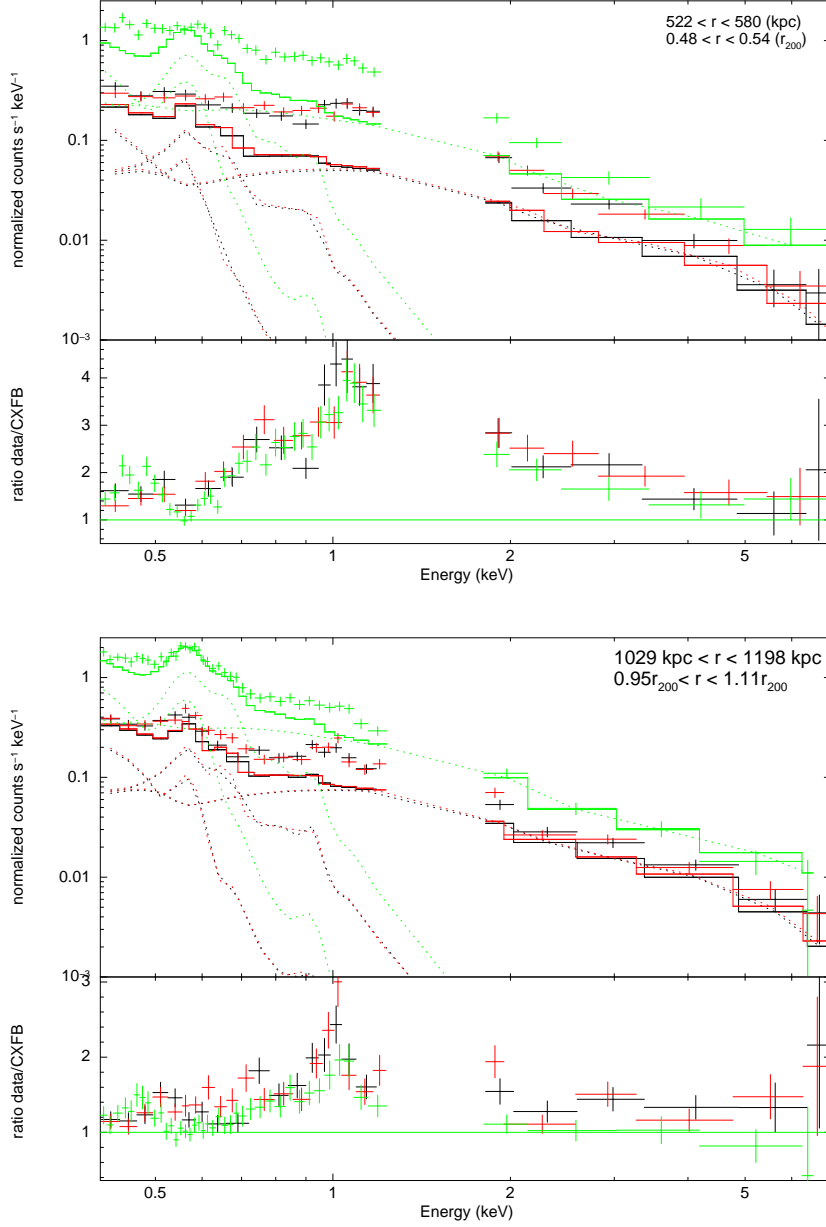


Figure 4.5: Examples of the analyzed spectra from $\sim 0.5 r_{200}$ and from $\sim r_{200}$. Data from all three EPIC instruments – MOS 1 (black), MOS 2 (red) and pn (green) – were fitted simultaneously. The figure shows the data with over-plotted CXFB model. Bottom part of each plot shows the ratio of the total to CXFB flux, thus indicating the amount of cluster emission.

In Fig. 4.7 we plot the bracketing values obtained as a result. Outside ~ 500 kpc the systematic errors dominate over the statistical, the values however remain well-determined and the trends robust.

The systematic error in the normalization of the instrumental background is 3 – 5%, arising mostly from the Poissonian error associated with the scaling factor used to account for the time-variation of the instrumental background. We simultaneously raised respectively lowered these factors by 1σ to achieve conservative estimate. The bracketing values are shown in Fig. 4.8, the trends once again remain robust.

4.3 Discussion

The results reported here are the first well-constrained spectroscopical measurements of the ICM properties in the outskirts of a dynamically young cluster. We compare them with the previous results from the simulations and the observations of hotter, more massive clusters.

4.3.1 The Unrelaxed Outskirts of a Forming Cluster

We measure an unusually shallow brightness profile along the northern arm of the cluster. In the $100 < r < 1000$ kpc region (outside the cold front) it can be fitted with a power-law $S_X \propto r^{-\alpha}$ with $\alpha = 1.34 \pm 0.01$. This is significantly less than $\alpha \sim 3$ in Abell 1795 (Bautz et al., 2009) or $\alpha \sim 3.6$ observed by *Chandra* between $0.4 - 0.7 r_{\text{vir}}$ in a sample of 52 $z > 0.3$ clusters (Ettori and Balestra, 2009). Low mass ($M_{\text{vir}} < 10^{15} M_{\odot}$) cluster simulations by Roncarelli et al. (2006) give the value of the ratio between the surface brightnesses at r_{vir} and $0.3 r_{\text{vir}}$ of 8×10^{-3} . The value of 0.16 measured for Virgo is more than an order of magnitude higher.

The electron density follows a power-law $n_e \propto r^{-\beta}$ with $\beta = 1.21 \pm 0.12$, a significantly shallower one than that for other authors. Simionescu et al. (2011) measure $\beta = 1.68 \pm 0.04$ in Perseus cluster, Bautz et al. (2009) give an even higher value of $\beta = 2.27 \pm 0.07$. Roncarelli et al. (2006) predict the value of β out to $\sim 1.2 r_{\text{vir}}$ to be 2.4 – 2.5.

Our temperature profile drops by $\sim 60\%$ between $0.3 - 1 r_{\text{vir}}$. This is in a good agreement with the previous measurements of the more massive clusters (Reiprich et al., 2009; Bautz et al., 2009; Hoshino et al., 2010; Simionescu et al., 2011). George et al. (2009) observe a drop by a factor of 4 in PKS 0745-191. Roncarelli et al. (2006) predict a drop by $\sim 40\%$, a prediction consistent also with the analytical result by Ostriker et al. (2005).

For the gravitationally collapsed gas in the hydrostatic equilibrium the hydrodynamical simulations (Tozzi and Norman, 2001; Voit, 2005) predict the entropy profile to obey a power-law $K \propto r^{1.1}$. Beyond ~ 450 kpc in Virgo the entropy however flattens out, remaining consistently lower from the expected value by a factor of 2 – 2.5. Other authors (George et al., 2009; Simionescu

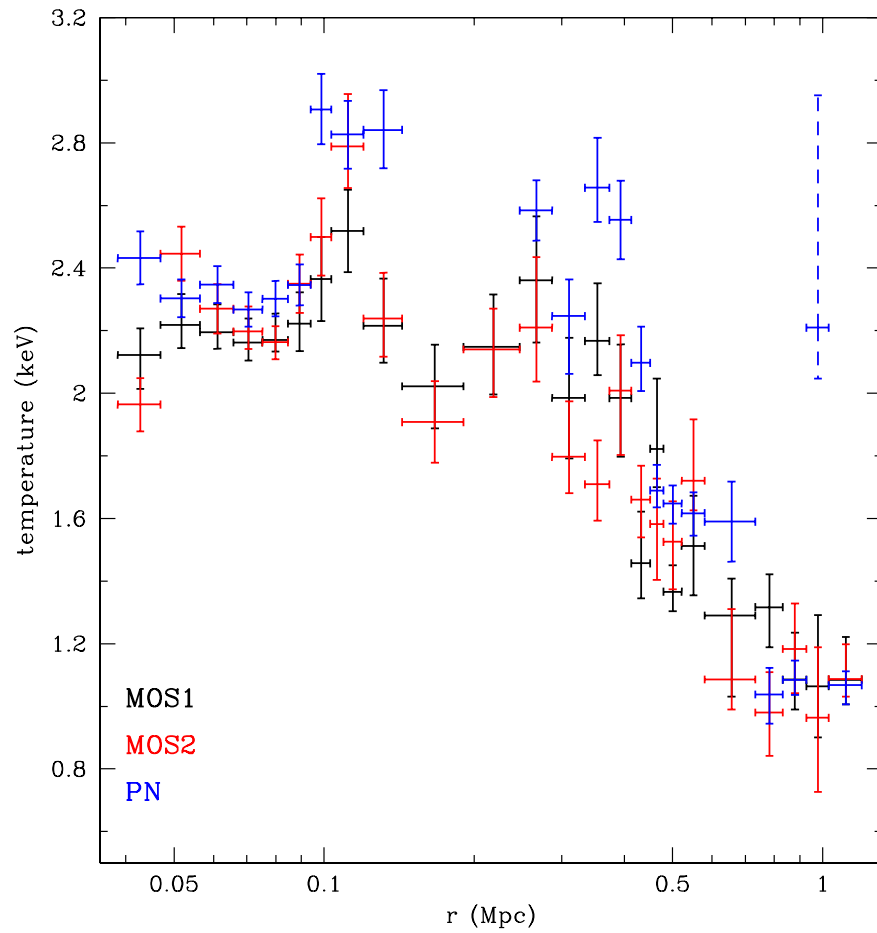


Figure 4.6: Temperature profiles for the separate EPIC instruments – MOS 1 (black), MOS 2 (red) and pn (blue). Dashed lines indicate the pn data that was not used.

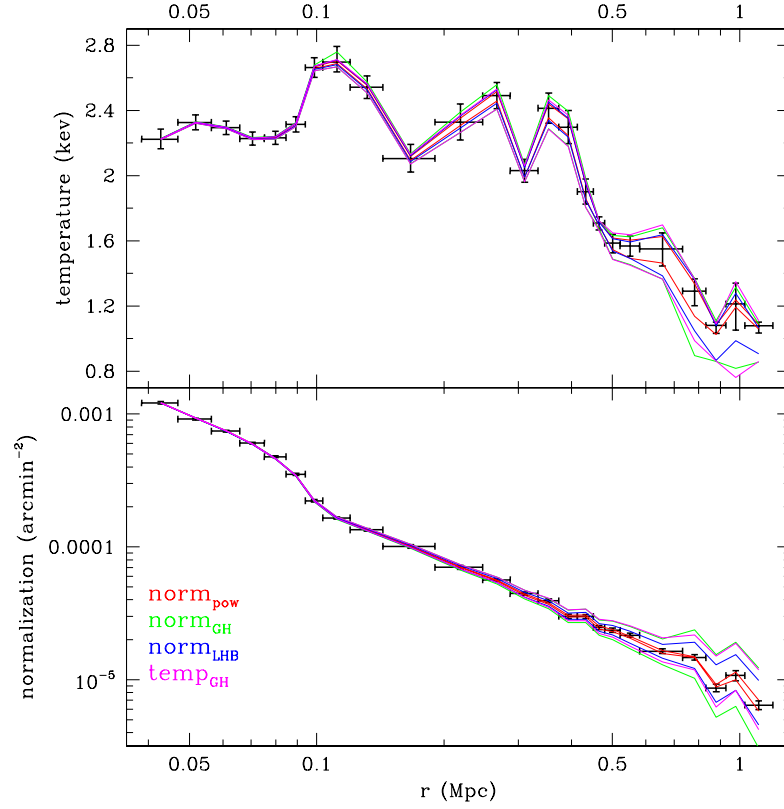


Figure 4.7: Projected temperatures (upper panel) and normalizations (lower panel) with over-plotted profiles obtained by varying CXB parameters (see the text for details). We show the bracketing values due to the uncertainties on the normalization of the power-law background component (norm_{pow}), normalization of the Galactic halo emission (norm_{GH}), normalization of the LHB emission component (norm_{LHB}), and the temperature of the Galactic halo emission component (temp_{GH}).

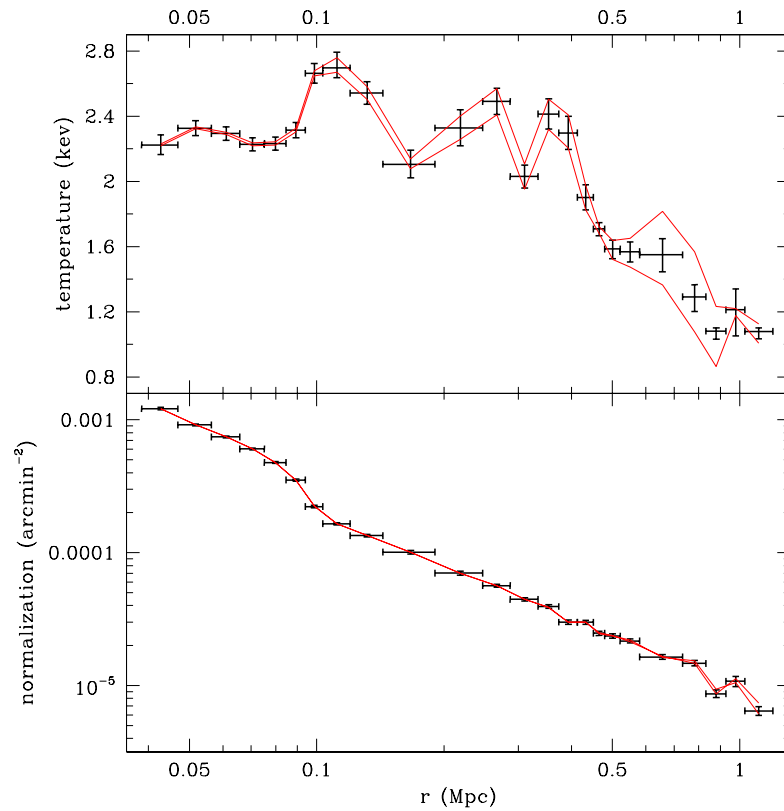


Figure 4.8: Projected temperatures (upper panel) and normalizations (lower panel) with over-plotted profiles obtained by varying the instrumental background (see the text for details).

et al., 2011) also report on the flattening of the entropy, however never at the radii this small.

Simionescu et al. (2011) show that the issues with the flattening of the entropy and also in their case the simultaneous apparent increase in the gas mass fraction above the cosmic mean in the outskirts of Perseus can be explained by the clumping of the ICM. The quantity obtained from the deprojected emission measure is average square of the density $\langle n^2 \rangle$, not the average density squared $\langle n \rangle^2$. The appearance of the non-uniform clumps in the ICM will therefore result in overestimation of the average density. If in addition the clumps are in the pressure equilibrium with the surrounding gas their temperature will be lower. The more plausible scenario however is for the clumps to be falling in the cluster being ram-pressure stripped. Depending on the ratio of the ram-pressure to thermal pressure support we would underestimate the temperature in the regions with clumps – denser and cooler blobs have higher volume emissivity. We see that increased clumping with the radius can therefore cause the flattening of the surface brightness profile, density profile and steepening of the temperature profile. The last two effects combined will then result in the observed flattening of the entropy in the outskirts.

Further test on the clumping hypothesis was done by simulating the *XMM-Newton* spectrum of two phase gas, both with $Z = 0.3 Z_{\odot}$. The 2 keV component represented the ambient ICM and the 1 keV one the clumps. We adjusted the emission measure so that the volume filling factor of the clumps would be $f = 0.2$, assuming pressure equilibrium (additional ram-pressure support would result in shrinking the volume filling factor). The simulated spectrum contained all the components of the background and had a similar statistical quality than the observed one. Fitting this spectrum with a single temperature model results in $kT = 1.24$ keV and the metallicity $Z = 0.16 Z_{\odot}$, about a factor of 2 lower than the real one. The density is overestimated by a factor of 1.6, thus the entropy inferred from this fit is about 2.2 times lower than the real ICM entropy, supporting the assumption of the clumping. The sudden decrease of the temperature beyond ~ 450 kpc can also be explained by this.

It is important to note that even though clumping offers itself as a natural explanation for the observed properties of the temperature, metallicity, density and the entropy, the real environment of the cluster is probably multiphase with clumps of slightly different temperatures that are probably partially ram-pressure confined.

An interesting further insight in the problem of clumping could be obtained from employing the SZ observations that, unlike the X-ray ones, depend linearly on n . This would result in discrepancy between the X-ray and SZ results. Assuming no biases in the temperature (complete ram-pressure support of the clumps so that they have the same temperature as their surroundings), we can infer the clumping factor by combining both observations. The interpretation may be complicated by the temperature biases arising from the multitemperature structure of the ICM.

4.3.2 Metals in the Outskirts

Our metallicity profile covers the whole cluster from the center out to the virial radius. Due to the relatively low ICM temperature the measurement is dominated mostly by Fe L complex of lines, thus the profile primarily shows the Fe abundance. In the $0.5 - 1 r_{\text{vir}}$ interval we see that the metallicity profile flattens out at a value of $\sim 0.1 Z_{\odot}$. As mentioned before, Fujita et al. (2008) measure the metallicity in the compressed outskirts of A 399/A 401 of $\sim 0.3 Z_{\odot}$. Recently published Simionescu et al. (2011) also obtain a similar result of $Z \sim 0.3 Z_{\odot}$.

As we describe in Sect. 4.3.1 the ICM in the cluster outskirts is probably multiphase with several components of various temperatures. It has been shown (see e.g. Buote (2000a), also our modelling in Sect. 4.3.1) metallicity can be sensitive to the incorrect modelling of the multiphase plasma. The Fe L emission line, which the most of our modelling depends on, is especially sensitive to the underlying temperature. Our resulting values should therefore be considered lower limits.

We can nevertheless use our best-fit values and assuming homogenous gas density and metal distribution we can calculate the cumulative Fe mass in the Virgo cluster. Using this method we obtain in the $0.1 - 1 r_{200}$ interval the total mass $M_{\text{Fe}} \sim 4 \times 10^9 M_{\odot}$, half of which can be found outside $0.5 r_{200}$. Due to the possible biases this estimate is most probably an underestimate. What we can relatively safely conclude however is that the total Fe mass outside $0.5 r_{200}$ is at least $2 \times 10^9 M_{\odot}$.

The question now stands how the ICM got polluted by metals to this level or alternatively how the metals got transported from the stars to the intracluster space. There are two main mechanisms of this – the galactic winds and the ram-pressure stripping. Galactic winds – also called super winds – are driven by the energy of numerous exploding supernovae (e.g. Heckman (2003)), thus they occur in the starburst regions. The main part of the enrichment from them happened at $z = 2 - 3$, where most of the star formation took place. The expelled pre-enriched gas got subsequently captured and fell into the cluster gravitational potential where, after having been shock heated, became a part of the ICM.

Fujita et al. (2008) argue for the galactic superwinds to be the main cause of the gas enrichment in A 399/A 401 region. Using the results of Fujita and Nagashima (1999) they claim that in order to reach the pressure of $\sim 2 \times 10^{-12}$ Pa needed to start the stripping of the gas from the galaxies they would need to reach the speed of $\sim 2000 \text{ km s}^{-1}$. Using the same argument the galaxies in Virgo would need to move with the unrealistic relative speeds of $\sim 3000 \text{ km s}^{-1}$ relative to the ICM for the process to take place. However looking at the H I maps of the Virgo cluster we can spot several galaxies in the interval of $0.6 - 1.2 \text{ Mpc}$ from the center of the cluster showing long H I tails (see e.g. Kenney et al. (2004); Chung et al. (2007); Kantharia et al. (2008)). In addition, the lower density, lower velocity dispersion environments like poor clusters or groups of galaxies also sometimes exhibit ram pressure stripping (e.g. Kantharia et al. (2005); Levy et al. (2007)). Simulations by Roediger and Brüggén (2007, 2008)

show that it is possible to strip gas even at the low ICM densities in the cluster outskirts due to the continuous or turbulent/vicious stripping (Nulsen, 1982). If an average completely stripped galaxy would provide $10^{10} M_{\odot}$ gas enriched to the solar metallicity it would take ~ 150 galaxies to be completely stripped of their gas to provide all the metals outside $0.5 r_{200}$. This would however introduce a radially decreasing profile, while both the Virgo and the Perseus metallicity are consistently flat.

Compared to the previous measurements the metallicity measured in the Virgo outskirts is significantly lower than expected. The only case of a similar result is the metallicity of $Z = 0.15 Z_{\odot}$ measured in the group NGC 5044 at $0.2 - 0.4 r_{\text{vir}}$ (Buote et al., 2004). Gonzalez et al. (2007) determine the ratio of the stellar versus ICM baryons to decrease with the increasing cluster mass, thus one would expect the metal enrichment of the ICM to decrease as well. The explanation of the higher metal content in the massive clusters would therefore be challenging. It is however possible to put this due to the multiphase biases as mentioned above. While the metallicity in the Virgo outskirts was mainly determined from Fe L lines, in the case of higher temperature clusters ($kT \gtrsim 3.5$ keV) this is done using Fe K lines. While the multiphase temperature structure could bias the metallicity in the latter case as well, the bias would be only up to $\sim 30\%$ (Rasia et al., 2008; Simionescu et al., 2009; Gastaldello et al., 2010).

5

Conclusions

In this thesis we dealt with the observational aspects of the galaxy clusters. In Chap. 1 we described the motivation to study these objects pointing out the plethora of interesting aspects they help us study focusing especially on their function as cosmological probes. Further on we discussed in detail the hot X-ray emitting gas, the ICM, filling the gravitational potential of the clusters and its various physical properties. Chap. 3 deals with the varying properties of the ICM across different parts of the clusters and how these variations help us learn more about the object itself. The chapter concludes with a brief discussion of the observations of the cluster outskirts and description of the *XMM-Newton* satellite used in the practical part of the thesis.

Chap. 4 comprises the whole practical part of the project. It is heavily based on Urban et al. (2011). We present there the first *XMM-Newton* observation of a modestly sized galaxy cluster – the Virgo cluster – out to and beyond the virial radius (out to $r \sim 1.2$ Mpc). The observations detect the cluster X-ray emission in all the pointings and enable us to study the structure of the ICM with unprecedented detail.

We observe unusually shallow surface brightness and density profiles. The temperature drops by $\sim 60\%$ between $0.3 - 1 r_{\text{vir}}$. Instead of following the theoretical dependence of $K \propto r^{1.1}$, outside ~ 450 kpc the entropy profile flattens out, keeping consistently lower than the expected value by a factor of $2 - 2.5$. It is also where both the temperature and metallicity drop abruptly.

These issues can most probably be explained by significant clumping of the ICM beyond ~ 450 kpc, that then rises with the increasing radius. The onset of the clumping appears at smaller scaled radius than that observed in the more massive Perseus Cluster (Simionescu et al., 2011).

Our measurements also give the value of the metallicity at the virial radius of $Z = 0.11 \pm 0.02 Z_{\odot}$. Given the above assumptions of clumping this value is most probably an underestimation and should be considered a lower limit.

The Virgo cluster, being the closest galaxy cluster, provides us with a unique chance to study the large scale structure of the Universe in detail. The results described here, those in Simionescu et al. (2011), their similarities and differences point to plenty of as-of-now unexplored areas of astrophysics and present an interesting challenge for the numerical simulations.

The results presented here were used when proposing future observations with all the most important X-ray observatories. Future promises even more detailed studies of the cluster outskirts and further exploration of the large-scale structure of the Universe and the cosmic web.

Bibliography

- G. O. Abell. The Distribution of Rich Clusters of Galaxies. *ApJS*, 3:211–+, May 1958. doi: 10.1086/190036.
- S. W. Allen, R. W. Schmidt, H. Ebeling, A. C. Fabian, and L. van Speybroeck. Constraints on dark energy from Chandra observations of the largest relaxed galaxy clusters. *MNRAS*, 353:457–467, September 2004. doi: 10.1111/j.1365-2966.2004.08080.x.
- S. W. Allen, D. A. Rapetti, R. W. Schmidt, H. Ebeling, R. G. Morris, and A. C. Fabian. Improved constraints on dark energy from Chandra X-ray observations of the largest relaxed galaxy clusters. *MNRAS*, 383:879–896, January 2008. doi: 10.1111/j.1365-2966.2007.12610.x.
- K. A. Arnaud. XSPEC: The First Ten Years. In G. H. Jacoby & J. Barnes, editor, *Astronomical Data Analysis Software and Systems V*, volume 101 of *Astronomical Society of the Pacific Conference Series*, pages 17–+, 1996.
- M. Arnaud, G. W. Pratt, R. Piffaretti, H. Böhringer, J. H. Croston, and E. Pointecouteau. The universal galaxy cluster pressure profile from a representative sample of nearby systems (REXCESS) and the Y_{SZ} - M_{500} relation. *A&A*, 517:A92+, July 2010. doi: 10.1051/0004-6361/200913416.
- M. W. Bautz, E. D. Miller, J. S. Sanders, K. A. Arnaud, R. F. Mushotzky, F. S. Porter, K. Hayashida, J. P. Henry, J. P. Hughes, M. Kawaharada, K. Makashima, M. Sato, and T. Tamura. Suzaku Observations of Abell 1795: Cluster Emission to r_{200} . *PASJ*, 61:1117–, October 2009.
- E. Belsole, J. L. Sauvageot, H. Böhringer, D. M. Worrall, K. Matsushita, R. F. Mushotzky, I. Sakelliou, S. Molendi, M. Ehle, J. Kennea, G. Stewart, and W. T. Vestrand. An XMM-Newton study of the sub-structure in M 87’s halo. *A&A*, 365:L188–L194, January 2001. doi: 10.1051/0004-6361:20000239.
- M. Birkinshaw and K. Lancaster. The Sunyaev-Zel’dovich Effect in Cosmology and Cluster Physics. In M. Plionis, O. López-Cruz, & D. Hughes, editor, *A Pan-Chromatic View of Clusters of Galaxies and the Large-Scale Structure*, volume 740 of *Lecture Notes in Physics*, Berlin Springer Verlag, pages 255–+, 2008.
- A. Biviano. From Messier to Abell: 200 Years of Science with Galaxy Clusters. In *Constructing the Universe with Clusters of Galaxies*, 2000.
- H. Böhringer and N. Werner. X-ray spectroscopy of galaxy clusters: studying astrophysical processes in the largest celestial laboratories. *A&ARv*, 18:127–196, February 2010. doi: 10.1007/s00159-009-0023-3.
- H. Böhringer, E. Belsole, J. Kennea, K. Matsushita, S. Molendi, D. M. Worrall, R. F. Mushotzky, M. Ehle, M. Guainazzi, I. Sakelliou, G. Stewart, W. T. Vestrand, and S. Dos Santos. XMM-Newton observations of M 87 and its X-ray halo. *A&A*, 365:L181–L187, January 2001. doi: 10.1051/0004-6361:20000092.

- M. Bradač, D. Clowe, A. H. Gonzalez, P. Marshall, W. Forman, C. Jones, M. Markevitch, S. Randall, T. Schrabback, and D. Zaritsky. Strong and Weak Lensing United. III. Measuring the Mass Distribution of the Merging Galaxy Cluster 1ES 0657-558. *ApJ*, 652:937–947, December 2006. doi: 10.1086/508601.
- U. G. Briel and J. P. Henry. An X-ray temperature map of the merging galaxy cluster A2256. *Nature*, 372:439–441, December 1994. doi: 10.1038/372439a0.
- D. A. Buote. Iron Gradients in Cooling Flow Galaxies and Groups. *ApJ*, 539:172–186, August 2000a. doi: 10.1086/309224.
- D. A. Buote. X-ray evidence for multiphase hot gas with nearly solar Fe abundances in the brightest groups of galaxies. *MNRAS*, 311:176–200, January 2000b. doi: 10.1046/j.1365-8711.2000.03046.x.
- D. A. Buote, F. Brighenti, and W. G. Mathews. Ultralow Iron Abundances in the Distant Hot Gas in Galaxy Groups. *ApJL*, 607:L91–L94, June 2004. doi: 10.1086/422097.
- E. T. Byram, T. A. Chubb, and H. Friedman. Cosmic X-Ray Sources-Galactic and Extragalactic. *AJ*, 71:379–+, August 1966. doi: 10.1086/109934.
- A. Chung, J. H. van Gorkom, J. D. P. Kenney, and B. Vollmer. Virgo Galaxies with Long One-sided H I Tails. *ApJL*, 659:L115–L119, April 2007. doi: 10.1086/518034.
- D. Clowe, A. Gonzalez, and M. Markevitch. Weak-Lensing Mass Reconstruction of the Interacting Cluster 1E 0657-558: Direct Evidence for the Existence of Dark Matter. *ApJ*, 604:596–603, April 2004. doi: 10.1086/381970.
- S. De Grandi and S. Molendi. Metallicity Gradients in X-Ray Clusters of Galaxies. *ApJ*, 551:153–159, April 2001. doi: 10.1086/320098.
- S. De Grandi and S. Molendi. Temperature Profiles of Nearby Clusters of Galaxies. *ApJ*, 567:163–177, March 2002. doi: 10.1086/338378.
- A. De Luca and S. Molendi. The 2-8 keV cosmic X-ray background spectrum as observed with XMM-Newton. *A&A*, 419:837–848, June 2004. doi: 10.1051/0004-6361:20034421.
- G. de Vaucouleurs. The Apparent Density of Matter in Groups and Clusters of Galaxies. *ApJ*, 131:585–+, May 1960. doi: 10.1086/146871.
- S. Ettori and I. Balestra. The outer regions of galaxy clusters: Chandra constraints on the X-ray surface brightness. *A&A*, 496:343–349, March 2009. doi: 10.1051/0004-6361:200811177.
- A. C. Fabian. Cooling Flows in Clusters of Galaxies. *ARA&A*, 32:277–318, 1994. doi: 10.1146/annurev.aa.32.090194.001425.

- A. C. Fabian, J. S. Sanders, G. B. Taylor, and S. W. Allen. A deep Chandra observation of the Centaurus cluster: bubbles, filaments and edges. *MNRAS*, 360:L20–L24, June 2005. doi: 10.1111/j.1745-3933.2005.00037.x.
- J. E. Felten and P. Morrison. Omnidirectional Inverse Compton and Synchrotron Radiation from Cosmic Distributions of Fast Electrons and Thermal Photons. *ApJ*, 146:686–+, December 1966. doi: 10.1086/148946.
- L. Feretti and G. Giovannini. Clusters of Galaxies in the Radio: Relativistic Plasma and ICM/Radio Galaxy Interaction Processes. In M. Plionis, O. López-Cruz, & D. Hughes, editor, *A Pan-Chromatic View of Clusters of Galaxies and the Large-Scale Structure*, volume 740 of *Lecture Notes in Physics*, Berlin Springer Verlag, pages 143–+, 2008.
- L. Feretti, I. M. Gioia, and G. Giovannini, editors. *Merging Processes in Galaxy Clusters*, volume 272 of *Astrophysics and Space Science Library*, June 2002.
- A. Finoguenov, L. P. David, and T. J. Ponman. An ASCA Study of the Heavy-Element Distribution in Clusters of Galaxies. *ApJ*, 544:188–203, November 2000. doi: 10.1086/317173.
- Y. Fujita and M. Nagashima. Effects of Ram Pressure from the Intracluster Medium on the Star Formation Rate of Disk Galaxies in Clusters of Galaxies. *ApJ*, 516:619–625, May 1999. doi: 10.1086/307139.
- Y. Fujita, N. Tawa, K. Hayashida, M. Takizawa, H. Matsumoto, N. Okabe, and T. H. Reiprich. High Metallicity of the X-Ray Gas Up to the Virial Radius of a Binary Cluster of Galaxies: Evidence of Galactic Superwinds at High-Redshift. *PASJ*, 60:343–+, January 2008.
- R. R. Gal. Optical Detection of Clusters of Galaxies. In M. Plionis, O. López-Cruz, & D. Hughes, editor, *A Pan-Chromatic View of Clusters of Galaxies and the Large-Scale Structure*, volume 740 of *Lecture Notes in Physics*, Berlin Springer Verlag, pages 119–+, 2008.
- F. Gastaldello, S. Ettori, I. Balestra, F. Brighenti, D. A. Buote, S. de Grandi, S. Ghizzardi, M. Gitti, and P. Tozzi. Apparent high metallicity in 3-4 keV galaxy clusters: the inverse iron-bias in action in the case of the merging cluster Abell 2028. *A&A*, 522:A34+, November 2010. doi: 10.1051/0004-6361/201014279.
- M. R. George, A. C. Fabian, J. S. Sanders, A. J. Young, and H. R. Russell. X-ray observations of the galaxy cluster PKS0745-191: to the virial radius, and beyond. *MNRAS*, 395:657–666, May 2009. doi: 10.1111/j.1365-2966.2009.14547.x.
- R. Giacconi, S. Murray, H. Gursky, E. Kellogg, E. Schreier, and H. Tananbaum. The Uhuru catalog of X-ray sources. *ApJ*, 178:281–308, December 1972. doi: 10.1086/151790.

-
- G. Giovannini, M. Tordi, and L. Feretti. Radio halo and relic candidates from the NRAO VLA Sky Survey. *Nature*, 4:141–155, March 1999. doi: 10.1016/S1384-1076(99)00018-4.
- A. H. Gonzalez, D. Zaritsky, and A. I. Zabludoff. A Census of Baryons in Galaxy Clusters and Groups. *ApJ*, 666:147–155, September 2007. doi: 10.1086/519729.
- N. Grevesse and A. J. Sauval. Standard Solar Composition. *Space Sci. Rev.*, 85:161–174, May 1998. doi: 10.1023/A:1005161325181.
- H. Gursky, E. Kellogg, S. Murray, C. Leong, H. Tananbaum, and R. Giacconi. A Strong X-Ray Source in the Coma Cluster Observed by UHURU. *ApJL*, 167:L81+, August 1971. doi: 10.1086/180765.
- H. Gursky, A. Solinger, E. M. Kellogg, S. Murray, H. Tananbaum, R. Giacconi, and A. Cavaliere. X-Ray Emission from Rich Clusters of Galaxies. *ApJL*, 173:L99+, May 1972. doi: 10.1086/180926.
- T. M. Heckman. Starburst-Driven Galactic Winds. In V. Avila-Reese, C. Firmani, C. S. Frenk, & C. Allen, editor, *Revista Mexicana de Astronomia y Astrofisica Conference Series*, volume 17 of *Revista Mexicana de Astronomia y Astrofisica Conference Series*, pages 47–55, June 2003.
- J. P. Henry and U. G. Briel. An X-ray temperature map of Abell 754: A major merger. *ApJL*, 443:L9–L12, April 1995. doi: 10.1086/187823.
- W. Herschel. O the Construction of the Heavens. *Royal Society of London Philosophical Transactions Series I*, 75:213–266, 1785.
- W. Herschel. Astronomical Observations Relating to the Construction of the Heavens, Arranged for the Purpose of a Critical Examination, the Result of Which Appears to Throw Some New Light upon the Organization of the Celestial Bodies. *Royal Society of London Philosophical Transactions Series I*, 101:269–336, 1811.
- A. Hoshino, J. Patrick Henry, K. Sato, H. Akamatsu, W. Yokota, S. Sasaki, Y. Ishisaki, T. Ohashi, M. Bautz, Y. Fukazawa, N. Kawano, A. Furuzawa, K. Hayashida, N. Tawa, J. P. Hughes, M. Kokubun, and T. Tamura. X-Ray Temperature and Mass Measurements to the Virial Radius of Abell 1413 with Suzaku. *PASJ*, 62:371–, April 2010.
- E. Hubble. A Relation between Distance and Radial Velocity among Extra-Galactic Nebulae. *Proceedings of the National Academy of Science*, 15:168–173, March 1929. doi: 10.1073/pnas.15.3.168.
- C. Jones and W. Forman. The structure of clusters of galaxies observed with Einstein. *ApJ*, 276:38–55, January 1984. doi: 10.1086/161591.

- C. Jones, W. Forman, A. Vikhlinin, M. Markevitch, M. Machacek, and E. Churazov. Dynamics of the Hot Intracluster Medium. In M. Plionis, O. López-Cruz, & D. Hughes, editor, *A Pan-Chromatic View of Clusters of Galaxies and the Large-Scale Structure*, volume 740 of *Lecture Notes in Physics*, Berlin Springer Verlag, pages 31–+, 2008.
- J. S. Kaastra and R. Mewe. An X-Ray Spectral Code for Optically Thin Plasmas, 1992. Internal SRON-Leiden Report, updated version 2.0.
- J. S. Kaastra, R. Mewe, and H. Nieuwenhuijzen. SPEX: a new code for spectral analysis of X & UV spectra. In K. Yamashita & T. Watanabe, editor, *UV and X-ray Spectroscopy of Astrophysical and Laboratory Plasmas*, pages 411–414, 1996.
- J. S. Kaastra, F. B. S. Paerels, F. Durret, S. Schindler, and P. Richter. Thermal Radiation Processes. *Space Sci. Rev.*, 134:155–190, February 2008. doi: 10.1007/s11214-008-9310-y.
- P. M. W. Kalberla, W. B. Burton, D. Hartmann, E. M. Arnal, E. Bajaja, R. Morras, and W. G. L. Pöppel. The Leiden/Argentine/Bonn (LAB) Survey of Galactic HI. Final data release of the combined LDS and IAR surveys with improved stray-radiation corrections. *A&A*, 440:775–782, September 2005. doi: 10.1051/0004-6361:20041864.
- N. G. Kantharia, S. Ananthkrishnan, R. Nityananda, and A. Hota. GMRT observations of the group Holmberg 124: Evolution by tidal forces and ram pressure? *A&A*, 435:483–496, May 2005. doi: 10.1051/0004-6361:20042261.
- N. G. Kantharia, A. P. Rao, and S. K. Sirothia. Low radio frequency signatures of ram pressure stripping in Virgo spiral NGC 4254. *MNRAS*, 383:173–182, January 2008. doi: 10.1111/j.1365-2966.2007.12525.x.
- J. D. P. Kenney, J. H. van Gorkom, and B. Vollmer. VLA H I Observations of Gas Stripping in the Virgo Cluster Spiral NGC 4522. *AJ*, 127:3361–3374, June 2004. doi: 10.1086/420805.
- K. D. Kuntz and S. L. Snowden. Deconstructing the Spectrum of the Soft X-Ray Background. *ApJ*, 543:195–215, November 2000. doi: 10.1086/317071.
- K. D. Kuntz and S. L. Snowden. The EPIC-MOS particle-induced background spectra. *A&A*, 478:575–596, February 2008. doi: 10.1051/0004-6361:20077912.
- L. Levy, J. A. Rose, J. H. van Gorkom, and B. Chaboyer. The Effect of Cluster Environment on Galaxy Evolution in the Pegasus I Cluster. *AJ*, 133:1104–1124, March 2007. doi: 10.1086/510723.
- D. A. Liedahl, A. L. Osterheld, and W. H. Goldstein. New calculations of Fe L-shell X-ray spectra in high-temperature plasmas. *ApJL*, 438:L115–L118, January 1995. doi: 10.1086/187729.

-
- D. N. Limber. Effects of Intracluster Gas and Duct upon the Virial Theorem. *ApJ*, 130:414–+, September 1959. doi: 10.1086/146733.
- R. Lynds and V. Petrosian. Giant Luminous Arcs in Galaxy Clusters. In *Bulletin of the American Astronomical Society*, volume 18 of *Bulletin of the American Astronomical Society*, pages 1014–+, September 1986.
- K. Matsushita, E. Belsole, A. Finoguenov, and H. Böhringer. XMM-Newton observation of M 87. I. Single-phase temperature structure of intracluster medium. *A&A*, 386:77–96, April 2002. doi: 10.1051/0004-6361:20020087.
- K. Matsushita, A. Finoguenov, and H. Böhringer. XMM observation of M 87. II. Abundance structure of the interstellar and intergalactic medium. *A&A*, 401:443–461, April 2003. doi: 10.1051/0004-6361:20021791.
- J. F. Meekins, G. Fritz, T. A. Chubb, and H. Friedman. Physical Sciences: X-rays from the Coma Cluster of Galaxies. *Nature*, 231:107–108, May 1971. doi: 10.1038/231107a0.
- C. Messier. Catalogue des nébuleuses et des amas d'étoiles que l'on découvre par les étoiles fixes, sur l'horizon de Paris, 1784.
- R. Mewe. Atomic Physics of Hot Plasmas. In J. van Paradijs & J. A. M. Bleeker, editor, *X-Ray Spectroscopy in Astrophysics*, volume 520 of *Lecture Notes in Physics*, Berlin Springer Verlag, pages 109–+, 1999.
- R. Mewe, E. H. B. M. Gronenschild, and G. H. J. van den Oord. Calculated X-radiation from optically thin plasmas. V. *A&AS*, 62:197–254, November 1985.
- R. Mewe, J. R. Lemen, and G. H. J. van den Oord. Calculated X-radiation from optically thin plasmas. VI - Improved calculations for continuum emission and approximation formulae for nonrelativistic average Gaunt factors. *A&AS*, 65: 511–536, September 1986.
- M. Milgrom. A modification of the Newtonian dynamics as a possible alternative to the hidden mass hypothesis. *ApJ*, 270:365–370, July 1983. doi: 10.1086/161130.
- R. J. Mitchell, J. L. Culhane, P. J. N. Davison, and J. C. Ives. Ariel 5 observations of the X-ray spectrum of the Perseus Cluster. *MNRAS*, 175:29P–34P, May 1976.
- S. Molendi. On the Temperature Structure of M87. *ApJ*, 580:815–823, December 2002. doi: 10.1086/343757.
- J. F. Navarro, C. S. Frenk, and S. D. M. White. A Universal Density Profile from Hierarchical Clustering. *ApJ*, 490:493–+, December 1997. doi: 10.1086/304888.

- D. M. Neumann. Tracing the X-ray emitting intra-cluster medium of clusters of galaxies beyond r_{200} . *A&A*, 439:465–477, August 2005. doi: 10.1051/0004-6361:20053015.
- P. E. J. Nulsen. Transport processes and the stripping of cluster galaxies. *MNRAS*, 198:1007–1016, March 1982.
- J. P. Ostriker, P. Bode, and A. Babul. A Simple and Accurate Model for Intracluster Gas. *ApJ*, 634:964–976, December 2005. doi: 10.1086/497122.
- U.-L. Pen. Measuring the universal deceleration using angular diameter distances to clusters of galaxies. *Nature*, 2:309–317, October 1997. doi: 10.1016/S1384-1076(97)00021-3.
- J. R. Peterson, F. B. S. Paerels, J. S. Kaastra, M. Arnaud, T. H. Reiprich, A. C. Fabian, R. F. Mushotzky, J. G. Jernigan, and I. Sakellou. X-ray imaging-spectroscopy of Abell 1835. *A&A*, 365:L104–L109, January 2001. doi: 10.1051/0004-6361:20000021.
- G. W. Pratt, H. Böhringer, J. H. Croston, M. Arnaud, S. Borgani, A. Finoguenov, and R. F. Temple. Temperature profiles of a representative sample of nearby X-ray galaxy clusters. *A&A*, 461:71–80, January 2007. doi: 10.1051/0004-6361:20065676.
- G. W. Pratt, J. H. Croston, M. Arnaud, and H. Böhringer. Galaxy cluster X-ray luminosity scaling relations from a representative local sample (REXCESS). *A&A*, 498:361–378, May 2009. doi: 10.1051/0004-6361/200810994.
- E. Rasia, P. Mazzotta, H. Bourdin, S. Borgani, L. Tornatore, S. Ettori, K. Dolag, and L. Moscardini. X-MAS2: Study Systematics on the ICM Metallicity Measurements. *ApJ*, 674:728–741, February 2008. doi: 10.1086/524345.
- T. H. Reiprich, D. S. Hudson, Y.-Y. Zhang, K. Sato, Y. Ishisaki, A. Hoshino, T. Ohashi, N. Ota, and Y. Fujita. Suzaku measurement of Abell 2204’s intracluster gas temperature profile out to 1800 kpc. *A&A*, 501:899–905, July 2009. doi: 10.1051/0004-6361/200810404.
- E. Roediger and M. Brüggen. Ram pressure stripping of disc galaxies orbiting in clusters - I. Mass and radius of the remaining gas disc. *MNRAS*, 380:1399–1408, October 2007. doi: 10.1111/j.1365-2966.2007.12241.x.
- E. Roediger and M. Brüggen. Ram-pressure stripping of disc galaxies orbiting in clusters - II. Galactic wakes. *MNRAS*, 388:465–486, August 2008. doi: 10.1111/j.1365-2966.2008.13415.x.
- E. Roediger, M. Brüggen, A. Simionescu, H. Böhringer, E. Churazov, and W. R. Forman. Gas sloshing, cold front formation and metal redistribution: the Virgo cluster as a quantitative test case. *MNRAS*, pages 369–+, March 2011. doi: 10.1111/j.1365-2966.2011.18279.x.

- M. Roncarelli, S. Ettori, K. Dolag, L. Moscardini, S. Borgani, and G. Murante. Simulated X-ray galaxy clusters at the virial radius: Slopes of the gas density, temperature and surface brightness profiles. *MNRAS*, 373:1339–1350, December 2006. doi: 10.1111/j.1365-2966.2006.11143.x.
- C. L. Sarazin. The Energy Spectrum of Primary Cosmic-Ray Electrons in Clusters of Galaxies and Inverse Compton Emission. *ApJ*, 520:529–547, August 1999. doi: 10.1086/307501.
- C. L. Sarazin. Gas Dynamics in Clusters of Galaxies. In M. Plionis, O. López-Cruz, & D. Hughes, editor, *A Pan-Chromatic View of Clusters of Galaxies and the Large-Scale Structure*, volume 740 of *Lecture Notes in Physics*, Berlin Springer Verlag, pages 1–4020, 2008.
- S. Sasaki. A New Method to Estimate Cosmological Parameters Using the Baryon Fraction of Clusters of Galaxies. *PASJ*, 48:L119–L122, December 1996.
- A. Scheepmaker, G. R. Ricker, K. Brecher, S. G. Ryckman, J. E. Ballintine, J. P. Doty, P. M. Downey, and W. H. G. Lewin. The Perseus and Coma clusters of galaxies at energies above 20 keV. *ApJL*, 205:L65–L68, April 1976. doi: 10.1086/182091.
- P. J. Serlemitsos, B. W. Smith, E. A. Boldt, S. S. Holt, and J. H. Swank. X-radiation from clusters of galaxies - Spectral evidence for a hot evolved gas. *ApJL*, 211:L63–L66, January 1977. doi: 10.1086/182342.
- S. D. Sidher, T. J. Sumner, J. J. Quenby, and M. Gambhir. Soft X-ray observations of the Galactic halo and the interstellar medium. *A&A*, 305:308–+, January 1996.
- A. Simionescu, H. Böhringer, M. Brüggen, and A. Finoguenov. The gaseous atmosphere of M 87 seen with XMM-Newton. *A&A*, 465:749–758, April 2007. doi: 10.1051/0004-6361:20066650.
- A. Simionescu, N. Werner, A. Finoguenov, H. Böhringer, and M. Brüggen. Metal-rich multi-phase gas in M 87. AGN-driven metal transport, magnetic-field supported multi-temperature gas, and constraints on non-thermal emission observed with XMM-Newton. *A&A*, 482:97–112, April 2008. doi: 10.1051/0004-6361:20078749.
- A. Simionescu, N. Werner, H. Böhringer, J. S. Kaastra, A. Finoguenov, M. Brüggen, and P. E. J. Nulsen. Chemical enrichment in the cluster of galaxies Hydra A. *A&A*, 493:409–424, January 2009. doi: 10.1051/0004-6361:200810225.
- A. Simionescu, N. Werner, W. R. Forman, E. D. Miller, Y. Takei, H. Böhringer, E. Churazov, and P. E. J. Nulsen. Metal transport by gas sloshing in M87. *MNRAS*, 405:91–99, June 2010. doi: 10.1111/j.1365-2966.2010.16450.x.

-
- A. Simionescu, S. W. Allen, A. Mantz, N. Werner, Y. Takei, R. G. Morris, A. C. Fabian, J. S. Sanders, P. E. J. Nulsen, M. R. George, and G. B. Taylor. Baryons at the Edge of the X-ray-Brightest Galaxy Cluster. *Science*, 331: 1576–, March 2011. doi: 10.1126/science.1200331.
- R. K. Smith, N. S. Brickhouse, D. A. Liedahl, and J. C. Raymond. Collisional Plasma Models with APEC/APED: Emission-Line Diagnostics of Hydrogen-like and Helium-like Ions. *ApJL*, 556:L91–L95, August 2001. doi: 10.1086/322992.
- S. L. Snowden and K. D. Knutz. Cookbook for Analysis Procedures for XMM-Newton EPIC MOS Observations of Extended Objects and the Diffuse Background. March 2010.
- S. L. Snowden, R. F. Mushotzky, K. D. Kuntz, and D. S. Davis. A catalog of galaxy clusters observed by XMM-Newton. *A&A*, 478:615–658, February 2008. doi: 10.1051/0004-6361:20077930.
- A. B. Solinger and W. H. Tucker. Relationship Between X-Ray Luminosity and Velocity Dispersion in Clusters of Galaxies. *ApJL*, 175:L107+, August 1972. doi: 10.1086/180996.
- G. Soucail, B. Fort, Y. Mellier, and J. P. Picat. A blue ring-like structure, in the center of the A 370 cluster of galaxies. *A&A*, 172:L14–L16, January 1987.
- L. Spitzer. *Physics of Fully Ionized Gases*. 1956.
- V. Springel, S. D. M. White, A. Jenkins, C. S. Frenk, N. Yoshida, L. Gao, J. Navarro, R. Thacker, D. Croton, J. Helly, J. A. Peacock, S. Cole, P. Thomas, H. Couchman, A. Evrard, J. Colberg, and F. Pearce. Simulations of the formation, evolution and clustering of galaxies and quasars. *Nature*, 435:629–636, June 2005. doi: 10.1038/nature03597.
- S. N. Stone. A Possible Extragalactic Source of 21-Centimeter Radio Emission. *PASP*, 67:183–185, June 1955. doi: 10.1086/126799.
- R. A. Sunyaev and Y. B. Zeldovich. The Observations of Relic Radiation as a Test of the Nature of X-Ray Radiation from the Clusters of Galaxies. *Comments on Astrophysics and Space Physics*, 4:173–+, November 1972.
- P. Tozzi and C. Norman. The Evolution of X-Ray Clusters and the Entropy of the Intracluster Medium. *ApJ*, 546:63–84, January 2001. doi: 10.1086/318237.
- J. A. Tyson, R. A. Wenk, and F. Valdes. Detection of systematic gravitational lens galaxy image alignments - Mapping dark matter in galaxy clusters. *ApJL*, 349:L1–L4, January 1990. doi: 10.1086/185636.
- O. Urban, N. Werner, A. Simionescu, S. W. Allen, and H. Böhringer. X-ray spectroscopy of the Virgo Cluster out to the virial radius. *MNRAS*, pages 546–+, April 2011. doi: 10.1111/j.1365-2966.2011.18526.x.

-
- S. van den Bergh. Collapsed Objects in Clusters of Galaxies. *Nature*, 224:891–+, November 1969. doi: 10.1038/224891a0.
- A. Vikhlinin, W. Forman, and C. Jones. Outer Regions of the Cluster Gaseous Atmospheres. *ApJ*, 525:47–57, November 1999. doi: 10.1086/307876.
- A. Vikhlinin, M. Markevitch, S. S. Murray, C. Jones, W. Forman, and L. Van Speybroeck. Chandra Temperature Profiles for a Sample of Nearby Relaxed Galaxy Clusters. *ApJ*, 628:655–672, August 2005. doi: 10.1086/431142.
- G. M. Voit. Tracing cosmic evolution with clusters of galaxies. *Reviews of Modern Physics*, 77:207–258, April 2005. doi: 10.1103/RevModPhys.77.207.
- L. Wang and P. J. Steinhardt. Cluster Abundance Constraints for Cosmological Models with a Time-varying, Spatially Inhomogeneous Energy Component with Negative Pressure. *ApJ*, 508:483–490, December 1998. doi: 10.1086/306436.
- N. Werner, H. Böhringer, J. S. Kaastra, J. de Plaa, A. Simionescu, and J. Vink. XMM-Newton high-resolution spectroscopy reveals the chemical evolution of M 87. *A&A*, 459:353–360, November 2006. doi: 10.1051/0004-6361:20065678.
- N. Werner, F. Durret, T. Ohashi, S. Schindler, and R. P. C. Wiersma. Observations of Metals in the Intra-Cluster Medium. *Space Sci. Rev.*, 134:337–362, February 2008a. doi: 10.1007/s11214-008-9320-9.
- N. Werner, A. Finoguenov, J. S. Kaastra, A. Simionescu, J. P. Dietrich, J. Vink, and H. Böhringer. Detection of hot gas in the filament connecting the clusters of galaxies Abell 222 and Abell 223. *A&A*, 482:L29–L33, May 2008b. doi: 10.1051/0004-6361:200809599.
- R. S. Wolff, H. Helava, T. Kifune, and M. C. Weisskopf. X-ray morphology of the Perseus cluster. *ApJL*, 193:L53–L56, October 1974. doi: 10.1086/181629.
- N. J. Woolf. On the Stabilization of Clusters of Galaxies by Ionized Gas. *ApJ*, 148:287–+, April 1967. doi: 10.1086/149148.
- F. Zwicky. On the Masses of Nebulae and of Clusters of Nebulae. *ApJ*, 86:217–+, October 1937. doi: 10.1086/143864.
- F. Zwicky. Non-Uniformities in the Apparent Distribution of Clusters of Galaxies. *PASP*, 69:518–+, December 1957. doi: 10.1086/127139.
- F. Zwicky, E. Herzog, and P. Wild. *Catalogue of galaxies and of clusters of galaxies*. 1968.